Department of Physics and Astronomy
Heidelberg University

Bachelor Thesis in Physics submitted by

Inna Shengying Zhang

born in Krefeld (Germany).

2024

Optimization of fiber-to-chip grating couplers on silicon-on-insulator platform

This Bachelor Thesis has been carried out by Inna Shengying Zhang
at the Kirchoff Institute für Physik (KIP) in Heidelberg
under the supervision of
Prof. Dr. Wolfram Pernice
and Dr. rer. nat. Simone Ferrari.

Abstract

With rapidly growing demands for data communication and processing, photonics offers a solution through faster data transfer, lower power consumption, and greater bandwidth. In this context, photonic integrated circuits have gained importance, particularly those based on the silicon-on-insulator (SOI) platform, which leverages high refractive index contrast for significant miniaturization and dense integration of optical components. However, SOI is inefficient at on-chip light generation, necessitating the introduction of optical signals from external sources. This need for hybridization, combined with the challenge of long-distance signal transmission, makes efficient fiber-to-chip coupling essential. While edge coupling provides a potential solution, low alignment tolerance and demanding fabrication procedure limits its applicability. Grating couplers offer a more scalable and efficient alternative, maintaining compatibility with standard fabrication processes and easing alignment. These structures facilitate vertical light coupling and enable convenient access to any location on the chip's surface, making them a highly attractive solution for coupling light between optical fibers and on-chip waveguides.

In this thesis work, I present the optimization of fiber-to-chip grating couplers on the silicon-on-insulator platform in the near infrared range. The focus is on optimizing the efficiency, working range and bandwidth of the grating coupler. A combination of full-vectorial 2D and 3D Finite-Difference Time-Domain simulations and Eigenmode Expansion simulations was employed to optimize both the grating and taper structures. The set of optimized parameters demonstrated in this work achieved a coupling efficiency of almost 60% at the target wavelength of 1550 nm, with a 3 dB bandwidth of 57 nm. These results guide the design of a chip, with planned experimental validation to to further enhance the grating coupler's performance in integrated photonic applications.

This page is left intentionally blank

Kurzfassung

Mit dem stark wachsenden Bedarf an Datenkommunikation und -verarbeitung bietet die Photonik eine Lösung mittels schnellerer Datenübertragung, geringeren Energieverbrauchs und größerer Bandbreite. In diesem Zusammenhang gewinnen photonische integrierte Schaltkreise zunehmend an Bedeutung, insbesondere solche, die auf der Silizium-auf-Isolator (SOI)-Plattform basieren. Diese ermöglicht aufgrund ihres hohen Brechungsindexkontrasts eine erhebliche Miniaturisierung und dichte Integration optischer Komponenten. Da SOI jedoch ineffizient bei der Lichtgeneration auf dem Chip ist, erfordert es die Einführung optischer Signale von externen Quellen. Der Bedarf an Hybridlösungen und die Herausforderung der Langstreckenübertragung machen eine effiziente Faser-zu-Chip-Kopplung unerlässlich. Kantenkoppler bieten zwar eine mögliche Lösung, haben jedoch eine geringe Toleranz gegenüber Ausrichtungsfehlern und erfordern aufwändige Herstellungsverfahren, was ihre Anwendbarkeit einschränkt. Gitterkoppler bieten eine skalierbare und effizientere Alternative, da sie mit standardisierten Herstellungsverfahren kompatibel sind und die Justage erleichtern. Diese Strukturen ermöglichen eine vertikale Lichtkopplung und einen einfachen Zugang zu verschiedenen Bereichen der Chipoberfläche, was sie zu einer attraktiven Lösung für die Kopplung von Licht zwischen optischen Fasern und Wellenleitern auf dem Chip macht.

In dieser Arbeit wird die Optimierung von Faser-zu-Chip-Gitterkopplern auf der SOI-Plattform im nahen Infrarotbereich vorgestellt. Der Fokus liegt auf der Optimierung der Effizienz, des Arbeitsbereichs und der Bandbreite der Gitterkoppler. Zur Optimierung der Gitter- und Taper-Strukturen wurde eine Kombination aus vollvektoralen 2D- und 3D-Finite-Difference-Time-Domain-Simulationen und Eigenmoden-Expansion-Simulationen verwendet. Die in dieser Arbeit ermittelten optimierten Parameter führten zu einer Kopplungseffizienz von fast 60% bei einer Zielwellenlänge von 1550 nm und einer 3-dB-Bandbreite von 57 nm. Diese Ergebnisse bilden die Grundlage für das Design eines Chips, dessen experimentelle Validierung zur weiteren Optimierung des Gitterkopplers für integrierte photonische Anwendungen vorgesehen ist.

This page is left intentionally blank

Contents

Chapter 1

Introduction

1.1 Motivation

The surge in data demand from mobile apps, video streaming, and cloud services is pushing telecommunications to new limits. Optical technologies have become crucial for meeting this demand by enabling high-bandwidth, long-distance data transmission [1]. To further push the boundaries of these capabilities, PICs have emerged as a transformative solution in optical systems [2]. PICs integrate multiple optical components, such as modulators and detectors, onto a single chip, which is pivotal for reducing system size and complexity, while enhancing scalability and lowering power consumption [3].

Among the various platforms for PICs, silicon photonics, particularly through the SOI platform, has emerged as a leading technology [4]. This prominence is driven by three primary factors. First, the high refractive index contrast between the silicon core ($n_{\mathrm{Si}} = 3.48$ at 1550nm [5]) and the SiO_2 cladding ($n_{\mathrm{SiO_2}} = 1.44$ at 1550nm [6]) in a SOI platform allows for strong light confinement, enabling the dense design of various optical components on a chip such as modulators, switches, and multiplexers [7]. Second, silicon's bandgap provides a broad transparency window over the communication channel (1.3 to 1.6 μm) [8]. Finally, the mature Complementary Metal-Oxide-Semiconductor (CMOS) fabrication infrastructure supports precise, scalable production of nanoscale devices, allowing for cost-effective mass manufacturing of PICs [9].

However, despite its advantages, SOI faces challenges, particularly due to silicon's indirect bandgap, which prevents efficient phonon-mediated radiative recombination, making it inefficient for on-chip light generation [10]. While efforts have been made with methods like quantum dots on silicon, lasing through doping, and plasmonic hybrid architectures, these approaches are either technically complex or suffer from low efficiency [11]. Therefore, silicon photonics requires hybrid approaches that combine different materials and technologies to address various challenges. This makes efficient coupling, both from external sources and chip-to-chip, crucial for progress [10]. Currently, fiber-to-chip coupling remains the most widely adopted solution to ensure efficient light transfer from external sources into the photonic circuits on the chip [12]. Given the significant size mismatch between standard single-mode fibers (SMFs), which typically have a mode field diameter (MFD) near 10 μm at 1550 nm, and silicon waveguides, which are on the scale of hundreds of nanometers, this coupling is nontrivial and presents challenges that must be addressed to minimize transmission losses [13].

1.2 Fiber-to-chip coupling methods in silicon photonics

To assess fiber-to-chip couplers, several key performance metrics must be considered. The two most critical are coupling efficiency (CE) and bandwidth (BW). CE measures the percentage of light transferred from the fiber into the waveguide, with higher CE indicating lower optical losses and better system performance. Bandwidth refers to the operating wavelength range over which the coupler operates efficiently, and a broader bandwidth is ideal for applications using multiple wavelengths, as it ensures stable performance despite variations in the operating wavelength, as well as coupling of multiple wavelengths at the same time for multiplexing [14].

Beyond these, other metrics include fabrication tolerance and operational tolerance. Fabrication tolerance encompasses factors like reproducibility, scalability, and footprint. Footprint refers to the physical size of the coupler, which is important in densely packed photonic circuits where space is limited. Designs with high fabrication tolerance account for the resolution limits of the nanofabrication process to ensure reliable performance and scalability in mass production. Operational tolerance considers factors like device access, stability over time, and translational and rotational alignment. Device access refers to the flexibility of placing the coupler at different points on the chip, which enhances design flexibility, while translational and rotational alignment reflect the coupler's sensitivity to misalignments between the fiber and the chip. Stability is crucial for maintaining performance over time, particularly in real-world conditions like temperature fluctuations and mechanical stress [15]. Finally, polarization dependence is another key factor, with low polarization dependence ensuring consistent performance regardless of the incoming light's polarization state [16].

Based on these metrics, several fiber-to-chip coupling methods have been developed to optimize performance [17]. A conceptual organization of different coupling structures is illustrated in Figure 1.1.

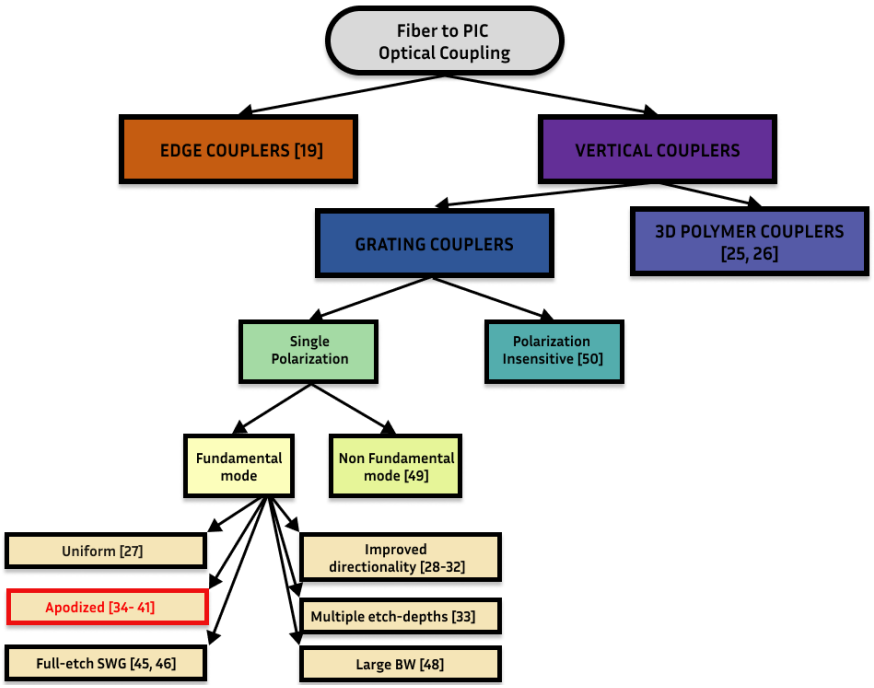

Figure 1.1: Conceptual organization of different methods proposed for optical coupling, the one discussed in this work highlighted in red.

Coupling methods are generally classified into two approaches: edge (or in-plane) coupling and vertical (out-of-plane) coupling [18]. Edge coupling involves placing the fiber at the chip facet

and aligning it horizontally with an inverse tapered waveguide, which gradually reduces the waveguide's width, allowing the mode size to expand and match the fiber mode [19]. Although edge coupling achieves high coupling efficiency and wide bandwidth, it restricts waveguide inputs to the chip's edge, limiting layout flexibility and increasing packaging complexity [20]. In contrast, vertical coupling allows more flexibility in photonic circuit design as inputs are no longer limited to the chip edge, freeing up space for additional photonic or electronic packaging and thus overcoming this limitation associated with in-plane approaches [21]. In this method, the light beam is incident from a fiber placed vertically or at a slight angle above the chip, where it is redirected into the waveguide by a specially designed structure, such as a grating coupler (GC).

Grating couplers are one of the most commonly used techniques among the various out-of-plane methods, relying on periodic planar structures to scatter the light out of the plane of the waveguide [22]. They are advantageous from a fabrication standpoint, owing to their high scalability, as they can be produced in the same step as the waveguide without requiring additional post-processing steps [23], as well as to their reduced footprint, which facilitates cost-effective wafer-level testing for large-scale production [24]. Despite these advantages, grating couplers tend to exhibit lower coupling efficiency and narrower bandwidth due to their sensitivity to wavelength and polarization, which can limit their application in certain use cases [18]. 3D-printed couplers offer an alternative, combining flexibility and scalability with improved coupling efficiency and broader bandwidth. These couplers use an adiabatic 3D polymer taper to interface with the 2D waveguide, followed by a mode-tapering section and a reflective lens to redirect light into the fiber [25]. While they outperform grating couplers in efficiency and bandwidth, their more complex fabrication process requires precise alignment and thus limits scalability and mechanical robustness [26].

In summary, while edge coupling methods offer high coupling efficiency and bandwidth, their limitations in layout flexibility and packaging complexity make them less ideal for dense or scalable circuits. Similarly, while 3D-printed couplers provide better performance, their fabrication complexity limits their practicality for mass production. Grating couplers, despite their sensitivity to bandwidth and polarization, offer a good trade-off between performance, ease of fabrication, and scalability. Their ability to be fabricated in the same step as waveguides, combined with their small footprint and compatibility with wafer-level testing, makes them highly suitable for use in SOI platforms, which is why they have been chosen as the coupling method studied in this work. In the next section a review of the current state-of-the-art for grating coupler strategies will be presented to help the reader better assess the performance of grating couplers, thus providing motivation for the objectives in this study, followed by an outline for this thesis work.

1.3 State-of-the-art for grating couplers

The maximum CE achieved by a standard uniform GC (UGC), which refers to a periodic refractive index variation, is generally below 60% [27]. To make up for the trade-offs in performance, several approaches have been made to improve performance while keeping the advantage of eased fabrication.

Among the various GC structures present in the literature to date, directionality enhancing designs, such as overlayer [28, 29] and back-reflector-assisted GC [30, 31, 32], and GCs with structural modifications are particularly widespread. Directionality-improving approaches have experimentally achieved CEs of up to 69% [28, 30, 31], but they require additional fabrication steps, which increase complexity and production costs. Similarly, multi-etch GCs, which

enhance performance by varying etch depths, despite some achieving up to 83.2% CE [33], introduce a trade-off in scalability and reproducibility due to the more complex fabrication process.

Apodized grating couplers (AGCs), on the other hand, are highly scalable and have competitive efficiency and cost-effective, simple fabrication processes, thus they represent the most attractive devices in terms of GCs with structural modification [22]. Apodization is a technique where grating parameters are varied along the length of the grating to control the coupling strength and thus shape the diffracted field to better match the Gaussian mode profile of the optical fiber. These techniques are often optimized through genetic algorithms (GA), which iteratively adjust the grating profile [34, 35, 36, 37], optimizing the CE through multiple simulated generations of potential configurations [38]. Currently to my best knowledge, the best experimental result with an apodized GC was achieved on a 260 nm thick SOI platform, reaching a CE of 81.3% [39], which is only slightly lower to that demonstrated in GC designs with more complex fabrication [33]. For a standard 220 nm thickness, the highest simulated and experimental CE values reach 72% [37] and 48.9% [40] respectively. A comparison between the different AGC in the standard 220nm SOI thickness is reported in Table 1.1.

GC Features	**Coupling Efficiency**		**Bandwidth [nm]**		**Reference**
	Sim.	**Exp.**	**Sim.**	**Exp.**	
AGC, GA, optimized BOX	61%	–	–	–	[36]
UGC	37%	31%	40^{A}	40^{A}	[27]
AGC+UGC, GP-chirp	42%	34%	48^{B}	45^{B}	[41]
AGC, GA, optimized BOX	72%	35%*	38^{A}, 64^{B}	$47^{A,*}$	[37]
AGC, FF-chirp	55%	48.9%	–	41^{A}	[40]
AGC, GA	61.9%	–	–	–	[34]
AGC, FF-chirp, varied GP	69.2%	–	–	–	[39]

^{A} 1dB Bandwidth. ^{B} 3dB Bandwidth. * Measured at 1536 nm.

Table 1.1: Comparison of coupling efficiencies and bandwidths reported in the literature for SOI grating couplers, in chronological order of release. Specifications include a standard 220 nm slab thickness, peak wavelength at 1550 nm, single layer fabrication, minimum feature size of 10nm and a Mode-Field-Diameter of 10.4 µm. Sim. stands for simulated and Exp. for experimental results. Grating Period (GP), Fill Factor (FF) and Bottom Oxide (BOX) refer to different grating parameters.

Various combinations of the aforementioned techniques have also been explored. For example, slanted grating couplers, composed of tilted grating sections [42, 43], or AGC combined with a backreflector in a genetic algorithm-optimized design on a 250 nm SOI platform, which achieved a record CE of 87% [44]. Other approaches include metamaterial-based GCs that use subwavelength structures or photonic crystals to reduce sensitivity to etch-depth fabrication errors [45, 46]. However again, these strategies all encompass more challenging fabrication, which has great impact in scalability and reproducibility. Another point to note is that higher efficiencies often come at the cost of reduced bandwidth [47], which has led to research on large-bandwidth GCs, such as those using aligned silicon nitride (SiN) and silicon grating teeth [48].

All GCs discussed in this section are 1D-GCs in the fundamental mode, which are optimized for a single-polarization state due to the high birefringence of SOI waveguides, making it challenging to efficiently couple both orthogonal polarization states in SMFs [11]. Recently, higher-order

mode coupling has gained interest, particularly in relation to spatial division multiplexing (SDM) technology, as it increases the information throughput of a single optical fiber, thus enhancing network capacity [49]. As for polarization-insensitive couplers, more complex designs are required [50], which is why single-polarization GCs remain more practical for applications requiring efficient coupling for a single polarization.

The research demonstrates that it is possible to design scalable grating couplers with competitive efficiency and cost-effective fabrication processes [34, 39]. For this reason, a single-step single-layer AGC is selected as the focus of this work.

1.4 Scope of this thesis

This work focuses on the development of GCs in the SOI platform, with the overarching goal to achieve high efficiency for the constraints imposed by our setup configuration and explore the parameters which allow to control efficiency, central wavelength and bandwidth. While the ideal goal is to achieve 100% coupling efficiency at 1550 nm, I set a performance threshold of no less than 50% efficiency for my application.

The choice of focusing my work on SOI is mainly due to two reasons. The first reason is its several advantages, as outlined in the motivation, including high refractive index contrast and compatibility with CMOS processes, which facilitate scalable fabrication and minimize the overall footprint of the devices. The second reason is that the SOI GC developed in this work can be embedded in several ongoing projects within the research group. One potential application of the developed grating coupler is in the Epique Project, which focuses on testing ultrafast waveguide-integrated superconducting nanowire single-photon detectors (SNSPDs). The high refractive index contrast of silicon allows ultrafast detectors to be easily embedded into compact photonic crystal cavities [51, 52]. This work provides a highly efficient method for coupling light onto the chip, an essential step in enabling the integration of these detectors within photonic circuits. Additionally, this research aligns with the goals of the NaPSAC (NanoWatt Platforms for Sensing, Analysis, and Computation) Project, an initiative by DARPA in collaboration with institutions such as EPFL and Purdue University [53]. The NaPSAC program focuses on developing ultralow power in-memory computing architectures. My contribution is therefore essential to allow efficent injection of the light in the photonic chip.

The next chapters are organized as follows:

In **Chapter 2** I provide a theoretical background on optical waveguides, grating couplers, and the numerical simulation methods used to analyze such structures. This includes the foundational concepts and equations governing the behavior of light in photonic structures, along with the design principles that guide grating coupler optimization.

In **Chapter 3**, the optimization and simulation configuration for the grating couplers are discussed in detail. Here, I present my approach to optimize grating couplers with respect to the preliminary constraints set by experimental conditions.

Chapter 4 presents the results of these simulations. The performance of various grating coupler and taper configurations are analyzed to determine optimal parameters.

In **Chapter 5**, I discuss future directions such as the fabrication of a photonic chip based on the optimized grating coupler designs. This chapter includes an outlook on next steps, including experimental testing and areas of improvement.

Finally, conclusions and a brief summary of the results obtained in this work are presented in **Chapter 6**.

Chapter 2

Theoretical Background

This chapter provides the essential theoretical background needed to understand photonic devices, laying the groundwork for the subsequent exploration of grating couplers and their application on the silicon-on-insulator platform. The basis for the coupling device studied in this thesis lays in the understanding of light propagation within photonic waveguides. Therefore, in ***Section 2.1****, I first discuss the nature of waveguides and the resonant mode solutions of the complex electric and magnetic field amplitudes. This is followed by an introduction to the theoretical framework of grating couplers in* ***Section 2.2****. Since this thesis focuses on optimizing these devices, I outline the key parameters that can be adjusted to enhance the performance of grating couplers in detail. In the final section,* ***Section 2.3****, I introduce the simulation methods used for the optimizations, EigenMode Expansion (EME) and Finite-Difference Time-Domain (FDTD).*

2.1 Guided optics

This section provides a fundamental overview of optical waveguides, focusing on the specific eigen-solutions for the electric and magnetic fields within the waveguide, which are referred to as modes. The reader is first presented with a description of waveguiding using ray optics, which provides an intuitive understanding based on total internal reflection. Following this, a more rigorous approach is introduced, where Maxwell's equations are directly used to describe the waveguide modes in detail.

2.1.1 Waveguides

Waveguides are the fundamental structures in photonics, designed to confine and guide light over a distance with minimal losses [54]. These structures, as illustrated in Figure 2.1, typically consist of a core region surrounded by cladding layers, with each layer distinguished by different materials and refractive indices.

The confinement of light within waveguides can be modeled in the ray optics picture using the principle of total internal reflection (TIR). Generally, TIR occurs when light traveling through a medium with a higher refractive index n_1 strikes the boundary with a medium of lower refractive index n_0 at an angle greater than the critical angle θ_c. This critical angle is determined by Snell's law, which reads [54]:

$$\theta_c = \sin^{-1}\left(\frac{n_0}{n_1}\right), \tag{2.1.1}$$

where n_1 is the refractive index of the higher-index medium and n_0 is the refractive index of the lower-index medium. When this condition is met, light is reflected back into the higher-index

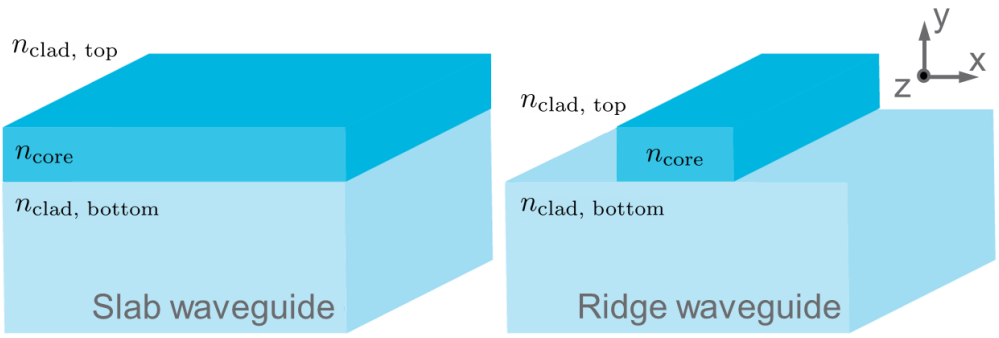

Figure 2.1: Schematic depiction of two different waveguide types with different layers of dielectric material. **Left:** Slab waveguide. **Right:** Ridge waveguide. n_{core} denotes the refractive index of the core region, while $n_{\text{clad, top}}$ and $n_{\text{clad, bottom}}$ denote the refractive indices of the top and bottom claddings, respectively. Adapted from [55].

medium. In the case of waveguides, the core acts as the higher-index medium with refractive index n_{core}, while the cladding layers, with refractive indices $n_{\text{clad, top}}$ and $n_{\text{clad, bottom}}$, serve as the lower-index media. For light to be guided within the core, the refractive indices must satisfy the condition [54]:

$$n_{\text{core}} > n_{\text{clad}}. \tag{2.1.2}$$

For a complete analysis of waveguides, the field distributions of the confined light, and thus the waveguide eigenmodes, must be considered. In this case, the description of waveguiding using ray analysis is insufficient, and an approach that directly applies Maxwell's equations proves more appropriate.

2.1.2 Wave Equation and Modes

The behavior of light as it travels is fundamentally described by Maxwell's equations in classical electrodynamics. These equations govern the interaction between electric and magnetic fields and their evolution over time and space, forming the basis for understanding light propagation in various optical components used in integrated photonics. In the context of light propagation in dielectric media, where there are no free charges or currents, Maxwell's equations read [56]:

$$\nabla \cdot \mathbf{E} = 0, \tag{2.1.3}$$
$$\nabla \cdot \mathbf{H} = 0, \tag{2.1.4}$$
$$\nabla \times \mathbf{E} = -\mu \frac{\partial \mathbf{H}}{\partial t}, \tag{2.1.5}$$
$$\nabla \times \mathbf{H} = \epsilon \frac{\partial \mathbf{E}}{\partial t}, \tag{2.1.6}$$

where $\mathbf{E}$ is the electric field, $\mathbf{H}$ is the magnetic field and μ and ϵ denote the permeability and permittivity of the medium, respectively. By applying the vector identity $\nabla \times (\nabla \times \mathbf{A}) = \nabla(\nabla \cdot \mathbf{A}) - \nabla^2 \mathbf{A}$ on the left-hand side of Equation 2.1.5 and Equation 2.1.6, Maxwell's equations can be decoupled to the wave equations in dielectric media [56]:

$$\nabla^2 \mathbf{E} - \mu\epsilon \frac{\partial^2 \mathbf{E}}{\partial t^2} = 0, \tag{2.1.7}$$
$$\nabla^2 \mathbf{H} - \mu\epsilon \frac{\partial^2 \mathbf{H}}{\partial t^2} = 0, . \tag{2.1.8}$$

In a homogeneous medium with constant permittivity and permeability, the solutions to the wave equation take the form of plane waves. Assuming the fields can be separated into transverse (x, y) and longitudinal (z) components, the solution for this plane wave propagating along the z-direction is [56]:

$$\mathbf{E}(z,t) = \mathcal{E}_0 e^{i(kz-\omega t)}, \tag{2.1.9}$$

where $\mathcal{E}_0$ is the complex amplitude of the wave, ω the angular frequency and $k = k_z = |\mathbf{k}|$ is the propagation constant in z-direction (with respect to Figure 2.1), also referred to as the wavenumber. Substituting Equation 2.1.9 into Equation 2.1.7 yields [57]:

$$k = \omega\sqrt{\mu\epsilon} = nk_0 \quad , \quad k_0 = \frac{\omega}{c}, \tag{2.1.10}$$

where k_0 is the free-space wavenumber and with the refractive index of the dielectric medium defined as [57]:

$$n \equiv \sqrt{\mu\epsilon}. \tag{2.1.11}$$

This can also be derived with the magnetic field wave equation or waves propagating in other directions. In many practical scenarios when dealing with a plane electromagnetic wave, it is characterised by its radiation wavelength λ, which is expressed by [58]:

$$\lambda = \frac{2\pi}{k} = \frac{\lambda_0}{n}, \tag{2.1.12}$$

where λ_0 represents the wavelength of the wave in free space. With the wave velocity along z-direction defined as $v = \frac{\omega}{k}$, the aforementioned wavenumber and refractive index can be written in gaussian units to:

$$k = \frac{2\pi n}{\lambda} = nk_0 \quad , \quad n = \frac{c}{v}. \tag{2.1.13}$$

These quantities are real values due to the assumption of the medium being perfectly dielectric. However generally they are complex quantities, with a factor accounting for absorption losses in the medium [59].

To accurately model the field distributions and propagation within waveguides, the more general solutions to the wave equations and thus the modes, given the refractive index does not vary in the z-direction, come in the form of [58]:

$$\mathbf{E}_\nu(x,y,z,t) = \mathcal{E}_\nu(x,y)e^{i(\beta_\nu z-\omega t)}, \tag{2.1.14}$$

$$\mathbf{H}_\nu(x,y,z,t) = \mathcal{H}_\nu(x,y)e^{i(\beta_\nu z-\omega t)}, \tag{2.1.15}$$

for the angular frequency ω. The eigenfunctions of each solution, differentiated by the index ν, are normalized complex amplitudes $\mathcal{E}_\nu$ and $\mathcal{H}_\nu$, which remain constant in the z-direction, again the defined direction of propagation. These define the mode profile, which can only be determined through numerical methods such as Finite Difference Methods (Chapter 2.3) as analytical solutions don't exist. The phase of these amplitudes is determined by the eigenvalues, known as the propagation constants β_ν. The propagation constant can also be expressed by an effective mode index n_{eff}, equivalently to the relation between the regular refractive index n and the wavenumber k of a plane wave [58]:

$$\beta = \frac{2\pi n_{\text{eff}}}{\lambda} = n_{\text{eff}}k_0 \quad , \quad n_{\text{eff}} = \frac{c}{v_{\text{eff}}}. \tag{2.1.16}$$

For slab waveguides as shown on the left of Figure 2.1, modes are denoted as follows [54]:

- Transverse Electric (TE) modes, where $\mathcal{E}_z = 0$ and $\mathcal{H}_z \neq 0$, and

- Transverse Magnetic (TM) modes, where $\mathcal{H}_z = 0$ and $\mathcal{E}_z \neq 0$.

However, this classification does not directly apply to ridge waveguides (shown on the right in Figure 2.1) due to the more complex boundary conditions of different media in the horizontal (x-) plane. Nevertheless, these waveguides support TE-like and TM-like modes [55]. TE-like modes have an electric field primarily oriented in the horizontal direction, while TM-like modes have a magnetic field mainly in the horizontal direction. For simplicity, the TE-like and TM-like modes in ridge waveguides are referred to as TE and TM modes in this thesis. Examples of the fundamental (0th order) eigenmodes are shown in Figure 2.2, where the magnitude of electric and magnetic fields is visualized through a color gradient, with red representing high values and blue representing low values. The field directions are indicated by white arrows.

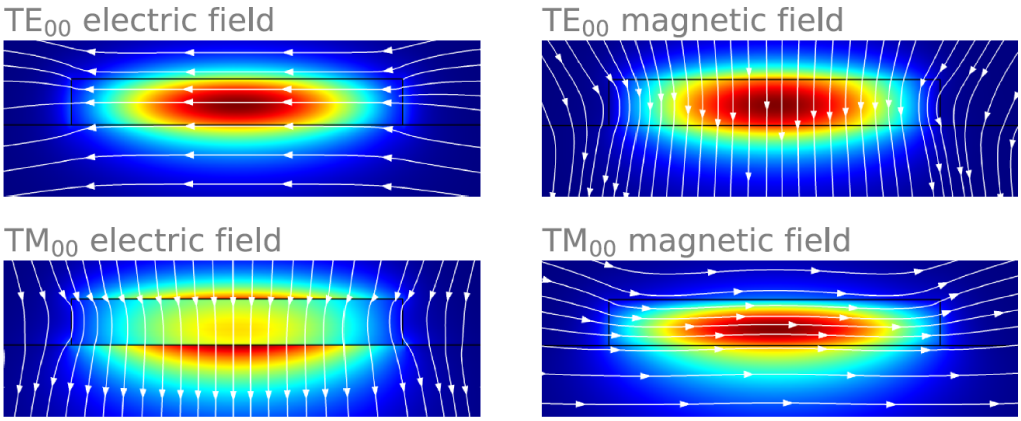

Figure 2.2: Visualization of TE-like and TM-like fundamental eigenmodes in the waveguide. The magnitude of the electric or magnetic field is represented by a color scale, with red indicating high values and blue indicating low values, while the field directions are shown by white arrows. [55]

The geometry of the waveguide and the refractive index contrast between the core and cladding dictate the number of supported modes. Higher refractive index contrast allows for more effective light confinement and can reduce the dimensions of the waveguide. This is particularly relevant when designing single-mode waveguides, where only the fundamental mode is supported. Single-mode waveguides are often preferred in applications like fiber optics, as they reduce intermodal dispersion and enhance signal clarity. By choosing a high refractive index material for the core and ensuring a sufficiently small core dimension, the waveguide can be designed to operate in the single-mode regime.

2.2 Grating Coupler

As prefaced in Chapter 1, the grating coupler (GC) is an optical device designed to couple light between an optical fiber and a planar waveguide. By adjusting the structural parameters of the GC, the efficiency of light transfer between the fiber and the waveguide can be optimized. This section provides a detailed explanation of how a grating coupler functions, what factors affect its performance, and what parameters can be optimized to improve CE and bandwidth.

2.2.1 Design

The functionality of a grating coupler is based on the diffraction of light by a periodic structure, typically composed of alternating regions of high and low refractive indices [22]. The grating

structure is integrated into the waveguide with a tapered structure, with the wafer constituting the grating coupler, which consists of a photonic waveguide-representative photo-conductive material, a buried oxide (BOX), and a substrate. A schematic of a 1D SOI incoupling GC is shown in Figure 2.3.

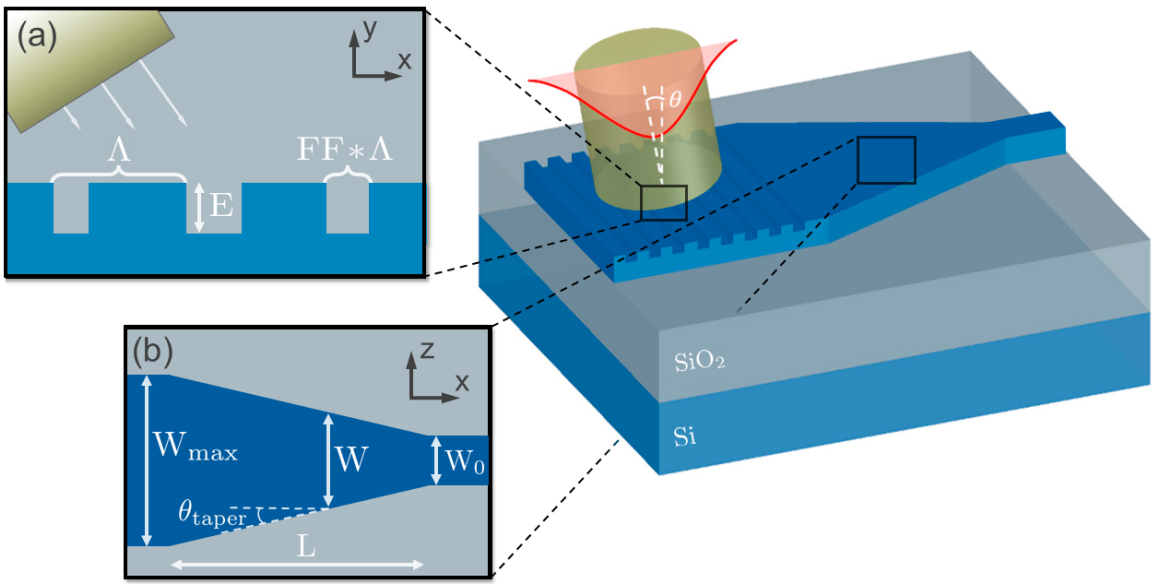

Figure 2.3: Schematic structure of a 1D SOI grating coupler as an incoupling device with a linear waveguide taper with zoom-ins on **(a)** the grating and **(b)** the taper structure. Right figure adapted from [22].

The primary structural parameters that define the **grating structure** are [60]:

- the grating period Λ, which is the distance between adjacent grating lines,
- the width of the grating teeth w,
- the fill factor FF, referring to the ratio of the unetched tooth width to the grating period,
- the etch depth E of the grating,
- the angle of diffraction θ_{clad} for outcoupling devices,
- and the angle θ_{fibre} for incoupling devices, which is the angle between the surface normal and the propagation direction of the incident light in the fiber.

with reference to Figure 2.3. When the refractive index is varied only along the direction of light propagation, the result is a 1D-GC; if varied along both the propagation direction and the waveguide width, a 2D-GC is realized. SOI waveguides typically exhibit high birefringence, making efficient coupling for both polarizations challenging [50]. As a result, 1D SOI GCs are usually optimized for a single polarization, offering simpler design and fabrication. TE-polarized light is preferred due to the anisotropic nature of the grating, which interacts more efficiently with TE than TM polarization [16].

The size mismatch between the MFD of an optical fiber and a waveguide necessitates the use of a **spot-size converter** in a grating coupler to gradually transition the optical mode from the large fiber mode into the smaller waveguide mode. A tapered waveguide serves this purpose by gradually adjusting the taper's width W along its length L, see in Figure 2.3(b). Different

designs such as linear, exponential, parabolic, or Gaussian tapers have been explored [61]. A linear taper design is further discussed is Chapter 2.2.3.

2.2.2 Coupling theory

The working principle of a GC is regulated by the Bragg condition, which dictates the diffraction of light in a periodic medium. Due to the reciprocity theorem which applies to linear open systems, both input and output GC configurations follow this principle [62]. For an outcoupling GC, the wave incident on the grating is a guided wave propagating in a slab waveguide with the waveguide propagation constant, as previously shown in Equation 2.1.16:

$$\beta = \frac{2\pi n_{\text{eff}}}{\lambda}. \tag{2.2.1}$$

The periodicity of the grating can be described by [60]:

$$K = \frac{2\pi}{\Lambda}, \tag{2.2.2}$$

where Λ is the grating period and higher-order diffraction gratings can be considered by $m \cdot K$. At the grating, the wave is diffracted, travelling in the cladding with a refractive index n_{clad} and the wavenumber [60]:

$$k = \frac{2\pi n_{\text{clad}}}{\lambda} \tag{2.2.3}$$

The Bragg condition in its general form can then be expressed as [22]:

$$k_x = \beta - m \cdot K, \tag{2.2.4}$$

where m is the grating diffraction order and k_x is the component of the wave vector of the diffracted wave in the direction of the incident wave, in this example the x-component of the wavevector $\mathbf{k}$:

$$k_x = k \cdot \sin\theta_{\text{clad}}, \tag{2.2.5}$$

with $k = |\mathbf{k}|$. It is also known as the phase-matching condition, as it showcases the relationship between the propagation constant β of the incident light wave in the waveguide and the wave vector k of the corresponding coupled light beam above the grating. By considering the first order diffraction angle, Equation 2.2.4 yields a version of the Bragg condition, in which one can directly see the dependency of the diffracted angle with the grating period and wavelength [18]:

$$\Lambda = \frac{\lambda}{n_{eff} - n_{\text{clad}} \sin\theta_{\text{clad}}}. \tag{2.2.6}$$

An important factor to consider is the relationship between the grating period and the wavelength of light within the grating material. If the index variation has a period larger than the wavelength $a > \lambda$, diffraction effects dominate, which is the desired regime for grating couplers. Otherwise, if the period is smaller $a < \lambda$, the propagation of light within the grating behaves similarly to a uniform medium, with this effect becoming more significant as the period decreases [22].

2.2.3 Linear taper

Ideally, the taper in a grating coupler operates adiabatically, meaning the light propagates through the taper while minimizing conversion to higher-order modes or radiation losses [61]. In cases where there is a significant difference between the initial and final waveguide widths,

as is typical in grating couplers, the taper must be extended to lengths of 300–500μm to ensure adiabatic propagation [22]. While longer tapers reduce mode conversion and improve efficiency, they occupy more chip area, which can be mitigated with compact taper designs that reduce footprint, such as focusing grating couplers [22]. These however come with the trade-off of additional factors to be minded. For a linear tapered waveguide, that allows adiabatic transition and a transmission of above 98%, the taper angle θ_{taper} is given by [61]:

$$\theta_{\text{taper}} = \alpha \frac{\lambda_0}{2W n_{\text{eff}}}, \tag{2.2.7}$$

where W is the varying taper width, n_{eff} is the corresponding mode effective index and $1 \leq \alpha \leq 1.4$ is a design parameter with respect to Figure 2.3(b). A smaller value of the design parameter α is selected when higher transmission is desired, as it minimizes mode conversion, but necessitates a longer taper. Conversely, a larger α reduces transmission efficiency, though it allows for a shorter taper. The length of the taper L, determined through geometric considerations, can be expressed as:

$$L = \frac{W_{\text{max}} - W_0}{2 \tan \theta_{\text{taper}}}, \tag{2.2.8}$$

where W_{max} represents the maximum taper width, corresponding to the grating width, and W_0 is the width of the single-mode waveguide. For a fixed length, the taper structure can be optimized by choosing an appropriate shaping profile parameter m to maximize transmittance while ensuring an optimal taper length, following [63]:

$$W(x) = \beta(L - x)^m + W_0, \tag{2.2.9}$$

$$W(0) = W_{\text{max}}, \tag{2.2.10}$$

$$W(L) = W_0, \tag{2.2.11}$$

$$\beta = \frac{W_{\text{max}} - W_0}{L^m}. \tag{2.2.12}$$

In this case, $m = 1$ represents the discussed linear taper shape.

2.2.4 Coupling Efficiency and Bandwidth

As mentioned in Chapter 1, one key figure of merit in evaluating a grating coupler's performance is its CE, which is essentially the fraction of incident light successfully coupled into the waveguide. To qualitatively estimate the CE, we can examine the main factors that contribute to reduced efficiency of a GC: penetration loss, mode mismatch, and back reflection [60]. The major power loss channels are illustrated in Figure 2.4.

For the input coupling scenario, first, a portion of the uncoupled power propagates downward, and generally about 30-50% of energy, denoted as P_{sub}, leaks into the substrate [36]. Second, a portion of the incident power P_{r} is reflected in the opposite direction of the input. Third, some power P_{w2} is coupled in the direction opposite to the desired waveguide propagation. In the case of perfect vertical incidence, the symmetry of the grating leads to bi-directional propagation of light, corresponding to the diffraction orders $m = 1$ and $m = -1$. To reduce the light diffracted in the opposite direction, the fiber is usually aligned at a slight angle rather than perfectly vertically. The final coupled power into the waveguide is given by [22]:

$$P_{\text{w}} = \eta_{\text{CE}} P_{\text{in}} = P_{\text{in}} - P_{\text{sub}} - P_{\text{r}} - P_{\text{w2}}, \tag{2.2.13}$$

where η_{CE} represents the coupling efficiency.

As for the chip-to-fiber out-coupling scenario, shown on the right side of Figure 2.4, the factors penetration loss and back reflection are present as well, with the addition of the modal mismatch

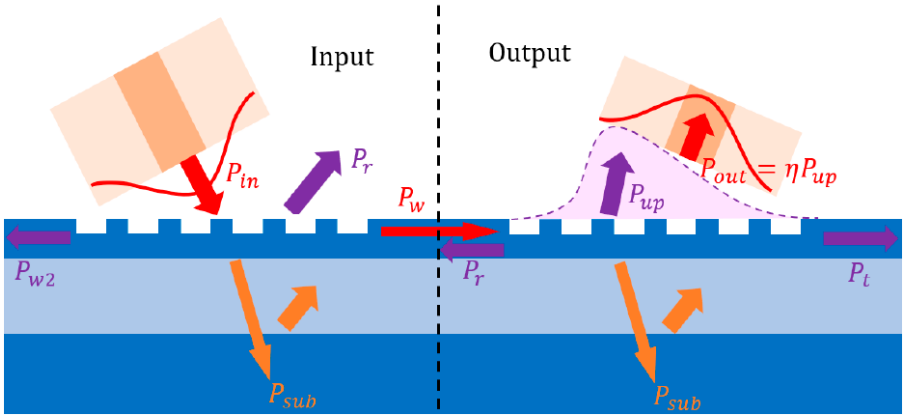

Figure 2.4: Loss channels in input and output coupling. [22].

factor. In this case, CE is typically characterized by directionality and modal overlap. Directionality $P_{\mathrm{up}}/P_{\mathrm{w}}$ refers to the fraction of waveguide power that diffracts upward towards the fiber. Backwards reflection arise here due to higher-order diffraction [60]. For shallow-etched grating couplers, back-reflections are typically small, however fully etched gratings can experience back-reflections as high as 30% [60]. As a result, grating couplers are seldom designed for vertical operation, with a small fiber tilt angle typically used for improved performance. Modal overlap refers to the portion of this upward-directed power that successfully couples into the fiber. The final coupled power into the fiber is given by [22]:

$$P_{\mathrm{out}} = \eta_{\mathrm{CE}} P_{\mathrm{w}} = \gamma(P_{\mathrm{w}} - P_{\mathrm{t}} - P_{\mathrm{r}}), \tag{2.2.14}$$

where γ is the overlap integral between the upward-directed mode profile $G(x)$ and the fiber mode profile $F(x)$, expressed as [22]:

$$\gamma = \frac{\int F(x)G(x)dx}{\int F^2(x)dx \int G^2(x)dx}. \tag{2.2.15}$$

The CE in GC can also be expressed in terms of coupling loss in decibels (dB), which is often used in literature. In this work we use the convention of reporting CE in percentage.

Beyond coupling efficiency, bandwidth (BW) plays a crucial role in defining a GC's operational range. Considering a deviation from the central wavelength λ_0, and assuming the effective index n_{eff} of the grating remains constant, the relationship between diffraction angle dispersion $\Delta\theta$ and wavelength shift $\Delta\lambda$ can be derived by substituting $\lambda = \lambda_0 + \Delta\lambda$ and $\theta = \theta_0 + \Delta\theta$ into Equation 2.2.6. This results in the following expression [64]:

$$\frac{\Delta\lambda}{\Delta\theta} = -\frac{\lambda_0 n_{\mathrm{clad}} \cos\theta_0}{n_{\mathrm{eff}} - n_{\mathrm{clad}} \sin\theta_0}. \tag{2.2.16}$$

For a single-mode fiber (SMF) with a given numerical aperture (NA), the allowed angular spread $\Delta\theta$ before the coupling efficiency drops by 1 dB is proportional to NA, assuming both the grating emission and fiber mode follow Gaussian profiles. Thus, the 1-dB bandwidth $\Delta\lambda_{1\mathrm{dB}}$ of the GC is given by:

$$\Delta\lambda_{1\mathrm{dB}} = C \cdot \mathrm{NA} \cdot \frac{\lambda_0 n_{\mathrm{clad}} \cos\theta_0}{n_{\mathrm{eff}} - n_{\mathrm{clad}} \sin\theta_0}, \tag{2.2.17}$$

where C is a constant. This expression suggests that decreasing the effective refractive index n_{eff} or increasing the incident angle θ_0 enhances the 1-dB bandwidth of the grating coupler [47]. Furthermore, accounting for the dispersion of the effective refractive index, reducing $\frac{dn_{\mathrm{eff}}}{d\lambda}$ also increases BW, as suggested in [65].

By understanding the factors that contribute to loss, specific design elements in GCs can be strategically adjusted to mitigate these inefficiencies. For instance, back reflectors can be introduced to reduce substrate leakage, while optimizing the grating period can address mode field mismatch. Such targeted modifications allow us to fine-tune the structure of the grating coupler and its surrounding environment. With these considerations in mind, the following section explores how parameters can be optimized to enhance CE, increase BW and tune the operational wavelength.

2.2.5 Key Parameters for Performance Optimization

The key parameters to enhance CE and adjust other important figures such as the central wavelength and bandwidth can be broadly classified into two categories: structural modifications to the grating coupler and other factors external to the grating itself, like the fiber characteristic and the BOX thickness. This subsection discusses both categories and their impact on CE and wavelength tuning.

The structure of the grating coupler directly affects the directionality of the light and the modal overlap. In terms of modifying the structure of the grating itself to enhance CE, a variety of **apodization techniques** have been proposed in the state-of-the-art [18], as discussed in Chapter 1.3. Single-step single-layer AGCs are favorable, as they don't require additional fabricational complexity. When only one parameter, such as the fill factor, is varied while the others are held constant, the AGC is referred to as linear apodization. If no parameters are varied, the grating is said to be uniformly apodized. In addition to enhancing CE, apodization can be used to tune other figures, such as the central wavelength. By fine-tuning the grating period, the grating coupler can achieve efficient light coupling at a specific wavelength, following the Bragg condition Equation 2.2.6.

The **etch depth** of the grating influences the effective refractive index of the diffracted light. As the etch depth increases, the effective refractive index n_{eff} decreases due to the larger proportion of light propagating in the low-index cladding. Since the central wavelength of the grating is proportional to n_{eff}, the central wavelength shifts to shorter wavelengths with increased etch depth [60]. Since both etch depth and apodization alter the effective index, they consequently affect the BW. In particular, greater etch depths and larger fill factors result in a lower effective index, thereby contributing to a broader BW.

In addition to structural factors, external parameters, such as **fiber characteristics**, significantly influence the performance of a GC. The incident angle, defined as the angle between the incoming light and the normal to the grating surface, affects both the mode matching between the fiber and the waveguide and the BW. A larger incident angle typically broadens the BW, as discussed in the previous section, while also impacting the central wavelength through the Bragg condition (see Equation 2.2.6). A positive incident angle indicates that the incident light and the coupled wave in the waveguide travel in the same direction, while a negative angle means they propagate in opposite directions [60]. Positive angle GC configurations focus the light primarily in the waveguide plane rather than in the outcoupling direction [66], which reduces the need for precise fiber alignment, allowing the fiber to approach the grating with less precision, making the setup more robust against mechanical shifts. Moreover, reducing angular dispersion can further broaden the BW, enabling the GC to operate over a wider wavelength range. This can be achieved either by using a SMF with a smaller MFD or by increasing the fiber's numerical aperture, allowing it to accept more dispersed light.

Finally, the **BOX thickness** affects the CE of the GC as well. Optimizing the BOX thickness can improve performance by reflecting some of the downward-propagating, uncoupled light back towards the waveguide through constructive interference, which can minimize absorption

in the substrate [37], thus enhancing CE in accordance with Equation 2.2.13.

2.3 Numerical Simulation Methods

Different numerical tools can be used to analyze and optimize structures in integrated photonics, such as grating couplers, that each come with advantages and trade-offs in relation to one another. The eigenmode expansion (EME) method divides a large structure into multiple parts and then propagates the solved eigenmodes of the parts in the frequency-domain, thus ideal for simulating light propagation over long distances [67]. The Finite-Difference Time-Domain (FDTD) method provides a time-domain solution to Maxwell's equations, making it ideal for broadband analysis and modeling complex photonic interactions [68]. This section explains the working principles of these numerical methods.

2.3.1 EigenMode Expansion (EME)

The EigenMode Expansion (EME) method models the bi-directional propagation of electromagnetic fields in the frequency-domain by dividing the waveguide structure into multiple sections and solving for the eigenmodes in each cross-section [69]. These eigenmodes, described by their mode profiles, effective indices, and propagation constants, are then propagated along the waveguide by calculating their interactions at boundaries, such as material discontinuities or geometrical changes.

In Chapter 2.2, Equation 2.1.14 and Equation 2.1.15, it was shown that the solutions to Maxwell's equations take the form of plane waves with harmonic z-dependence, assuming the refractive index is constant along the z-direction and a single wavelength and time dependence of the form $e^{i\omega t}$:

$$\mathbf{E}(x, y, z) = \mathcal{E}_\nu(x, y)e^{i\beta_\nu z}. \tag{2.3.1}$$

Typically, waveguides support a few guided modes that propagate without loss, along with an infinite number of radiation modes that carry optical power away from the waveguide, such as into the substrate layer [70]. The guided and radiation modes together form a complete basis set, and any solution of Maxwell's Equations in a given region of the waveguide can be expressed as a superposition of forward and backward propagating modes [71]:

$$\mathbf{E}(x, y, z) = \sum_\nu \mathcal{E}_\nu(x, y) \left(a_\nu^{(+)} e^{i\beta_\nu z} + a_\nu^{(-)} e^{-i\beta_\nu z}\right), \tag{2.3.2}$$

$$\mathbf{H}(x, y, z) = \sum_\nu \mathcal{H}_\nu(x, y) \left(a_\nu^{(+)} e^{i\beta_\nu z} - a_\nu^{(-)} e^{-i\beta_\nu z}\right), \tag{2.3.3}$$

where $\mathcal{E}_\nu$ and $\mathcal{H}_\nu$ are the electric and magnetic field profiles, β_ν is the propagation constant, and $a_\nu^{(+)}$, $a_\nu^{(-)}$ are the amplitudes of the forward and backward propagating modes, respectively. This set of equations provides an exact solution to Maxwell's equations in a linear medium, assuming an infinite summation.

In the EME method, light propagation is computed by first solving for the eigenmodes in each cross-section, then propagating these modes along the waveguide and calculating their interactions at boundaries. At each boundary, as illustrated in Figure 2.5, Maxwell's continuity conditions between the mode coefficients hold, which yields the relationship [70]:

$$\begin{pmatrix} a_\nu^{(-)} \\ b_\nu^{(+)} \end{pmatrix} = \mathbf{S} \begin{pmatrix} a_\nu^{(+)} \\ b_\nu^{(-)} \end{pmatrix}, \tag{2.3.4}$$

where $a_\nu^{(+)}$ and $a_\nu^{(-)}$ are the amplitudes of the modes entering and exiting the left-hand side, respectively, and $b_\nu^{(+)}$ and $b_\nu^{(-)}$ are the corresponding right-hand side amplitudes. The scattering matrix S contains the transmission and reflection coefficients at the boundary. The main approximation for this relationship to hold, is that the sum in Equation 2.3.2 and Equation 2.3.3 must be truncated to a finite number of modes. Typically, accuracy can be preserved by selecting an appropriate number of modes [70].

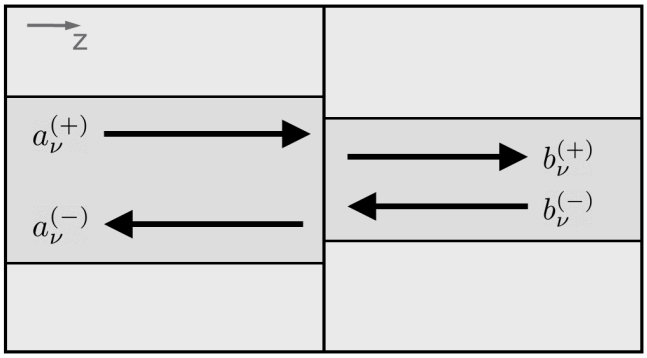

Figure 2.5: Schematic illustration of mode coefficients at the interface between two waveguides. Adapted from [70].

The EME method is particularly effective for structures with gradual geometric changes along the propagation direction, such as the spot size converter analyzed in this work. Because EME operates in the frequency domain, it avoids the time-stepping required by time-domain methods like Finite-Difference Time-Domain (FDTD), making it computationally efficient. However, for more complex structures like grating couplers, where the geometry varies more, EME becomes insufficient. In such cases, methods like FDTD, which resolve the full time-domain behavior of the fields, are more suitable.

2.3.2 Finite-Difference Time-Domain (FDTD)

The **Finite-Difference Time-Domain (FDTD)** method directly solves Maxwell's equations by discretizing both space and time [68], making it highly accurate for handling more complex structures, such as grating couplers. Operating in the time domain, FDTD is particularly effective for broadband simulations, as it captures electromagnetic wave propagation across a wide frequency range. By solving Maxwell's curl equations in this discretized framework, FDTD accurately models electromagnetic interactions in complex photonic structures [54].

Expanding Maxwell's curl equations (Equation 2.1.5 and Equation 2.1.6) into six equations for the time derivatives of the electric field **E** and magnetic field **H** components for each spatial direction reads [72]:

$$\begin{aligned}
\frac{\partial E_x}{\partial t} &= \frac{1}{\epsilon}\left(\frac{\partial H_z}{\partial y} - \frac{\partial H_y}{\partial z}\right), & \frac{\partial H_x}{\partial t} &= \frac{1}{\mu}\left(\frac{\partial E_y}{\partial z} - \frac{\partial E_z}{\partial y}\right), \\
\frac{\partial E_y}{\partial t} &= \frac{1}{\epsilon}\left(\frac{\partial H_x}{\partial z} - \frac{\partial H_z}{\partial x}\right), & \frac{\partial H_y}{\partial t} &= \frac{1}{\mu}\left(\frac{\partial E_z}{\partial x} - \frac{\partial E_x}{\partial z}\right), \\
\frac{\partial E_z}{\partial t} &= \frac{1}{\epsilon}\left(\frac{\partial H_y}{\partial x} - \frac{\partial H_x}{\partial y}\right), & \frac{\partial H_z}{\partial t} &= \frac{1}{\mu}\left(\frac{\partial E_x}{\partial y} - \frac{\partial E_y}{\partial x}\right).
\end{aligned} \tag{2.3.5}$$

The FDTD method uses a staggered grid, known as the Yee grid [73], where the electric and magnetic field components are calculated at alternating spatial and temporal points. Starting

from an initial field distribution, the electric field components are updated at each time step, followed by the calculation of the magnetic field components in a leapfrog manner [72]. This iterative process continues until the fields stabilize or the desired simulation time is reached. In comparison to the EME method, the FDTD method directly captures the coupling between electric and magnetic fields, offering more accurate light propagation simulations through less approximations, though it is computationally intensive due to the extensive calculations required at each time step.

The key parameters that influence the computational load in FDTD simulations include the mesh size, time step, and iteration time. The mesh size determines the resolution at which material properties, geometrical information, and the electric and magnetic fields are calculated at each mesh point [67]. Finer mesh sizes are essential for capturing nanometer-scale features, particularly those found in the grating couplers studied here. However, smaller mesh sizes significantly increase memory usage and computation time. Thus, selecting an appropriate mesh size balances accuracy with computational efficiency. Similarly, the time step and iteration time must be carefully chosen in time-domain methods like FDTD to ensure stability and convergence without excessive computational costs.

Conclusion

With the theoretical foundation in place, these principles can be applied to the design and optimization of grating couplers. Concepts such as effective refractive index, waveguide mode propagation, and the Bragg condition form the basis for configuring grating structures. The importance of tuning parameters like apodization, incident angle and taper length has been highlighted as critical to achieving efficient coupling. In the subsequent simulation work, I will use the Bragg condition to fine-tune the grating design, and I will optimize the taper geometries based on the linear taper relationship.

Chapter 3

Methods

This chapter details the methods used to design and optimize a high-efficiency SOI grating coupler. I begin by defining the initial conditions in ***Section 3.1****, which include fabrication and experimental constraints such as the 220 nm SOI wafer and the 100 nm minimum feature size, as well as the 8° fiber array polishing angle. In* ***Section 3.2****, I outline the optimization procedure, which was constrained by the aforementioned limitations. Finally, in* ***Section 3.3****, I describe the use of 2D- and 3D-FDTD simulations, along with the EME Solver. I employed these tools to model the grating structures and taper geometry, with consideration given to balancing computational accuracy and efficiency by adjusting mesh sizes and boundary conditions.*

3.1 Preliminaries

The initial conditions for the grating coupler simulation are defined by a combination of fabrication constraints and setup requirements. One primary constraint is the use of a SOI material stack, featuring a 220 nm crystalline silicon top layer and a BOX layer with a thickness of 2.2 μm. The 220 nm thick wafers are readily available to our research group and were selected to ensure compatibility with standard CMOS photonic processes, as this silicon thickness is an industry standard. Additionally, as mentioned in Section 1.4, our group has previously developed a set of functioning devices such as photonic crystal cavities and SNSPDs on this platform, further justifying the use of this material stack. To ensure high reproducibility, a conservative minimum feature size limit of 100 nm was imposed. While the electron beam lithography (E-beam) process offers a resolution capability of 10 nm, the variability inherent in the etching process and potential resist thickness variations led to this larger feature size buffer, contributing to more reliable device fabrication.

An additional constraint arises from the experimental setup, which uses a fiber array with a fixed polishing angle of 8° that the grating coupler must accommodate to ensure efficient light coupling. This angle directly impacts the design of the grating structure, as it influences the diffraction angle in accordance with Equation 2.2.6 and, consequently, the coupling efficiency. The central wavelength of 1550 nm was selected due to its widespread use in telecommunications, as well as our existing device set, which is designed to operate at this wavelength. The grating coupler must be designed to match our SMF-28 1550 nm in-house fiber array MFD [74] of 10.4 μm for light at this wavelength.

Taking these initial conditions into consideration, the steps to reach the performance goal presented in Section 1.4 can be determined. It is to mention that while these conditions are guided by fabrication limitations and experimental constraints, the approach itself is not limited to such a subset. The methods employed in this work can be adapted to different initial conditions.

3.2 Optimization procedure

To establish a baseline for the grating coupler design, I reference the work of Bozzola et al. [34], in which the authors achieved one of the highest simulated coupling efficiencies up to date of 64.65% at 1550 nm, using an optimized apodized grating structure. For the CMOS-constrained design with a 220 nm thickness, a CE of 61.9% was obtained. A cross-sectional schematic of this optimized design is shown in Figure 3.1.

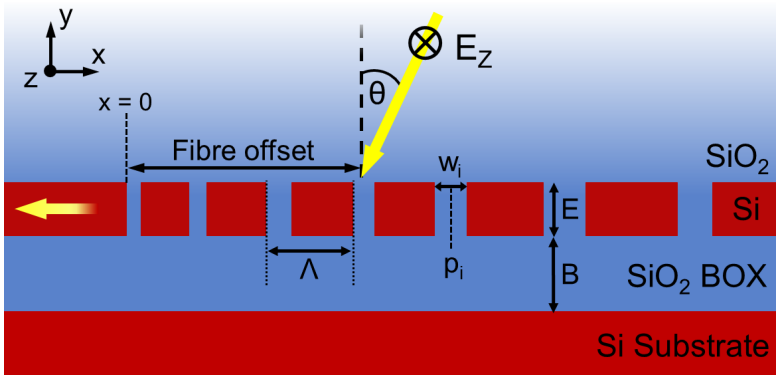

Figure 3.1: Cross-sectional schematic layout of an apodized 1D GC in a SOI wafer. Adapted from [34].

The design features 23 grating teeth and 24 grating gaps with a full etch depth of $E = 220$ nm, a BOX thickness of $B = 2200$ nm, a top oxide layer for protection. The in-coupling fibre is tilted by θ=10° with respect to the vertical direction, its offset is optimized to 4.2 μm from the first grating trench and the electric field of the beam is polarized along the z-direction, so that the incoming light is coupled to the fundamental TE mode of the integrated waveguide. The optimized silicon dioxide bar positions p_i are plotted over the grating index in blue on the left-hand side of Figure 3.2. For the interested reader, the precise configuration of the grating positions p_i and widths w_i can be referred to in Table 1 of [34].

Since the design from [34] is engineered for an incident angle of 10°, the GC needs to be modified to accommodate for the 8° polishing angle of our fiber array. The Bragg condition (see Equation 2.2.6) shows that changing only the diffraction angle would influence the coupling-wavelength as well, making it deviate from the target wavelength of 1550nm. Instead, this work takes the approach of modifying the grating period to meet the target wavelength at a different angle. Through observation of the grating positions, it becomes evident that the structure can be well approximated by a linear trend. This suggests that by approximating the grating periods to a constant value, the CE may be optimized for the 8° incident angle, as shown in red on the left of Figure 3.2. The approximation results in a linear grating design, where both the grating period and the fill factor $\mathrm{F} = \frac{w_i}{\Lambda}$ remain constant. The other structural parameters, such as the grating widths, BOX thickness, and etch depth, are retained from the original design. A schematic comparison of the optimized and linearly approximated grating structures is illustrated on the right of Figure 3.2, where (a) represents the original optimized design and (b) depicts the new linear approximation.

Following the verification of the grating design, the grating's lateral size and taper geometry are optimized. While focusing configurations can reduce the footprint of a GC, the high effective index of the SOI platform in this case already ensures a compact design without the added complexity in the lateral dimension. Therefore, a square-shaped GC with a linear taper was selected for conformity. Typically, the width of the grating ($W_{\max}$ in Figure 2.3(b)) is chosen to be about 12μm to accomodate the Gaussian beam emitted by a SMF with a MFD of 10.4μm [27].

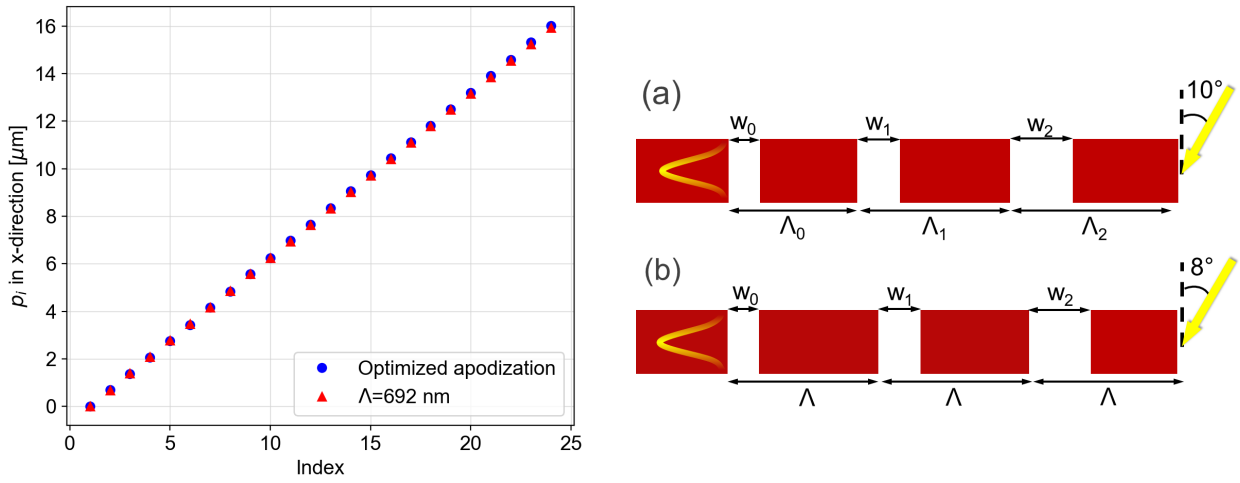

Figure 3.2: Comparison between the optimized and linear grating designs. **Left:** Grating positions p_i plotted against the grating index for the optimized apodization and linear approximation, with a constant grating period $\Lambda = 692$ nm. **Right:** Schematic representation of the original optimized (a) and the linearly approximated (b) grating structures.

An adiabatic taper, with a length L (see Figure 2.3(b)) of at least 150 μm, connects the grating to the single-mode waveguide [31]. To minimize footprint while maintaining performance, these initial parameters guide the optimization of the 3D GC design. In an additional step, the impact of different taper shapes on the performance of the taper was explored. The results from each optimization step combined gave a final grating coupler design for validation.

3.3 Simulation Setup

Simulations in this work were conducted using FDTD Solutions® and MODE Solutions® from ANSYS Inc. [75]. The initial grating design, as well as the linearly approximated grating design that accommodates the 8° fiber angle of the experimental setup, was validated using 2D-FDTD simulations, which provided an efficient way to explore an initial design in two dimensions. Following this, 3D-FDTD simulations were conducted to optimize the grating width, addressing the lateral dimension, which cannot be accounted for in 2D simulations. The taper geometry was then refined using the EME solver to vary the taper length and shape, providing insight into transmission efficiency for different configurations. Finally, a complete grating coupler design, including the determined optimized parameters, was simulated in 3D to validate the overall device performance. A flowchart summarizing the overall optimization process is shown in Figure 3.3. The following section details the specific simulation configurations used for optimizing the grating coupler.

3.3.1 Finite-Difference Time-Domain Simulations

For the verification of the initial grating design and its linear approximated version, full vectorial 2D-FDTD simulations were performed. While grating couplers are inherently three-dimensional, the majority of the complexity in the third dimension arises from the tapering transition to the smaller waveguide. In the case of a straight coupler, the structure remains two-dimensional in rectangular coordinates and extends uniformly into the third dimension [76]. Therefore, the grating was approximated in two dimensions for simulation purposes. Once the design was validated, full vectorial 3D-FDTD simulations were used to account for the lateral

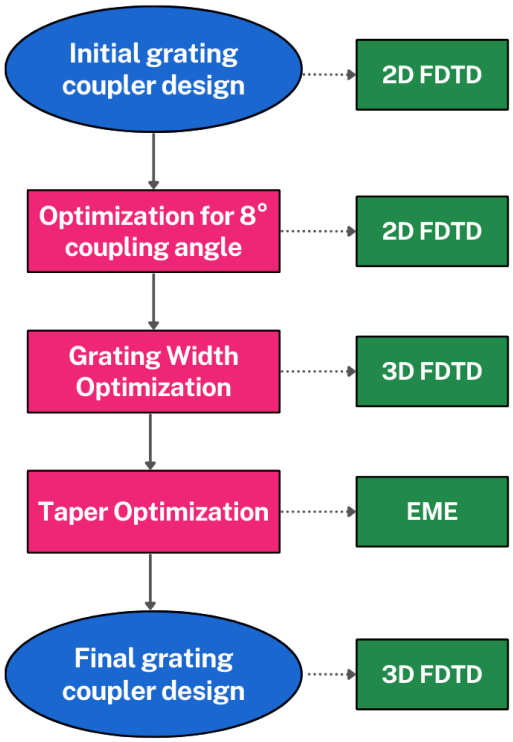

Figure 3.3: Flowchart of the design process in the scope of this work. The blue circles mark the starting and end points, the pink squares represent the optimization steps, and the green squares indicate the simulation methods used at each step.

size of the device. These simulations provide greater accuracy by accounting for the full geometry of the coupler, albeit with significantly higher computational demands due to the large number of calculations at every time step [68]. To balance accuracy and efficiency, simulation parameters such as mesh size, boundary conditions, and symmetry planes were carefully chosen, ensuring reliable results without excessive computational overhead.

As a rule of thumb the mesh size is chosen to be approximately the center wavelength divided by 8, which balances accuracy with computational efficiency. In addition to mesh size, boundary conditions (BCs) also impact the computational load and accuracy of FDTD simulations. In this work, Perfectly Matched Layer (PML) boundaries were applied at the simulation edges to absorb outgoing waves and prevent reflections at the boundaries from distorting the fields inside the domain. Symmetry BCs were applied within the simulation region to further reduce computational demands when the electromagnetic fields exhibited a plane of symmetry [77]. When the electric field component normal to the symmetry plane was zero, symmetric BCs were used, while anti-symmetric BCs were implemented when the magnetic field component normal to the plane was zero. By leveraging the symmetry of the grating coupler design, the computational domain size was reduced, decreasing simulation time without affecting accuracy.

To evaluate the performance of the grating couplers, a frequency-domain power monitor was placed within the simulation domain to capture the electromagnetic field data across a designated cross-section or line. This monitor calculates the transmitted and reflected power for each frequency, allowing the CE to be determined as the ratio of transmitted power to incident power. Additionally, the monitor can analyze far-field projections, including the angular distribution of transmission.

The corresponding 2D-FDTD simulation set up to the discussed GC design in Section 3.2 is shown in Figure 3.4(a). The grating is first simulated as an in-coupling device with a gaussian

source, which mimics the mode of a single-mode fiber, coupling light into the SOI waveguide through the GC. The beam is assumed to have a distance from waist of 1μm and a Mode-Field-Diameter of 10.4μm. The yellow line represents the frequency-domain power monitor, positioned along the Si waveguide at a 10μm distance from the grating. Figure 3.4(b) shows the simulation setup for the GC as an outcoupling device. In this case a fundamental TE mode source is placed within the SOI waveguide, and the power monitor is positioned above the GC to assess its directionality. The 3D-FDTD simulation for the optimization of the grating width

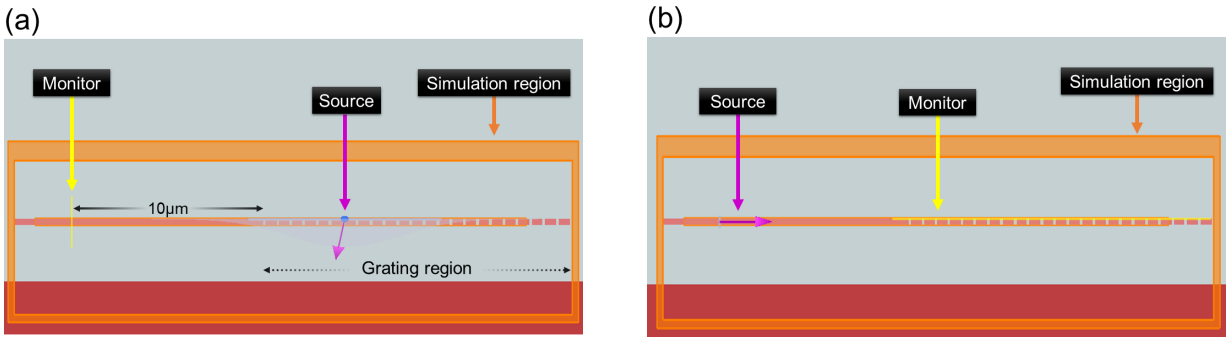

Figure 3.4: 2D-FDTD simulation configuration for the GC as an **(a)** incoupling device and **(b)** outcoupling device.

focuses on the grating region within the simulation region, which is marked in Figure 3.4(a). Later for the simulation of a complete in-coupling GC device, the simulation region as well as the monitor is extended to fit the taper.

3.3.2 EME Solver Simulations

The EME solver was employed to study how transmission varies with the taper's length and shape, with the goal of optimizing the geometry for maximum transmission into the fundamental mode. Specifically, a linear taper was simulated, consisting of a trapezoidal waveguide connecting two waveguides of different widths. The waveguide and background material, as well as the emission wavelength, were chosen to match the parameters used in previous FDTD simulations. Anti-Symmetry and Symmetry conditions were applied to leverage the symmetry of the structure. Two ports were set up at each end of the taper structure. To calculate transmission, the solver computes the scattering (S-) matrix as described in Equation 2.3.4, which contains the transmission and reflection coefficients between the waveguide ports. For the fundamental TE mode, so a single mode per port, the S-matrix is a 2×2 matrix [78]:

$$\mathbf{S} = \begin{pmatrix} S_{11} & S_{12} \\ S_{21} & S_{22} \end{pmatrix} \tag{3.3.1}$$

Here, the indices refer to the port numbers, with S_{21} representing the transmission coefficient from input Port 1 to output Port 2, and S_{12} representing the transmission in the reverse direction. S_{11} and S_{22} are the reflection coefficients at Ports 1 and 2, respectively. By performing parameter sweeps of the taper's length and shape, the transmission can be optimized by maximizing the total power transferred from the input to the output, quantified as $|S_{12}|^2$.

Conclusion

This chapter has provided a comprehensive overview of the methodology employed to design and optimize a high-efficiency SOI grating coupler. By integrating 2D- and 3D-FDTD simulations

with the EME solver, the grating structure and taper geometry was systematically refined while adhering to fabrication constraints. These methods balanced practical design limitations with high performance.

In the next chapter, I present the simulation results and evaluate the grating coupler designs in terms of coupling efficiency and bandwidth, assessing the impact of these optimizations on overall device performance.

Chapter 4

Results

*In this chapter, the results of the undertaken simulations are presented. In **Section 4.1**, I first reproduced the result presented in literature for the 10° angle as validation. I then adapted the initial design to meet our experimental requirements and constraints using a linearly approximated approach in **Section 4.2**, specifically optimizing for an 8° incident angle while maintaining similar performance. Additionally, I explored the engineering of the grating's lateral size and the tapering geometry of the coupling section to seamlessly match the waveguide width in **Section 4.3** and **4.4**, respectively. Lastly, in **Section 4.5**, I simulated a complete grating coupler design to validate the overall device performance.*

4.1 Simulation of an initial grating coupler design

The initial grating coupler design adapted from [34] was first verified in a 2D-FDTD simulation as shown in Figure 3.4(a). The resulting transmission spectrum is shown in Figure 4.1, where the maximum CE reaches 64.18% at 1550 nm with a 1dB BW of 31.8 nm and a 3dB BW of 55.3 nm, confirming the optimised accuracy of the grating position and width values as reported by Bozzola et al. [34]. The relatively broad BW, particularly the 3dB BW, indicates strong performance across a wider wavelength range, while the peak efficiency at 1550 nm aligns with the design objective and serves as a validation of the optimized apodized grating structure for further study.

The E-field cross-sectional distributions of the grating coupler at the peak wavelength of 1550 nm and a non-optimal wavelength of 1700 nm are illustrated in Figure 4.2(a) and (b) respectively. The E-field distribution at 1550 nm shows effective light propagation through the waveguide with minimal reflection as expected for this wavelength. In contrast, the E-field distribution at 1700 nm exhibits significant reflection in the grating structure with a substantial portion of the light absorbed in the substrate, leading to reduced coupling efficiency and increased losses.

To get a complete analysis of the optimized apodized GC design, the grating was also simulated as an out-coupling device, see Figure 3.4(b). Figure 4.3(a) and (b) illustrate the far-field projection and far-field angular profile at a wavelength of 1550 nm, respectively. The peak emission angle is observed to shift linearly with wavelength, consistent with the Bragg condition. Furthermore the intensity reaches a low point at an angle of 0°, confirming the second-order diffraction back into the waveguide discussed in Chapter 2. The far-field profile at 1550 nm demonstrates a maximum electric field intensity at an emission angle of 10°, with the intensity following a Gaussian distribution as a function of angle.

The simulation results of the in-coupling as well as the out-coupling device altogether demon-

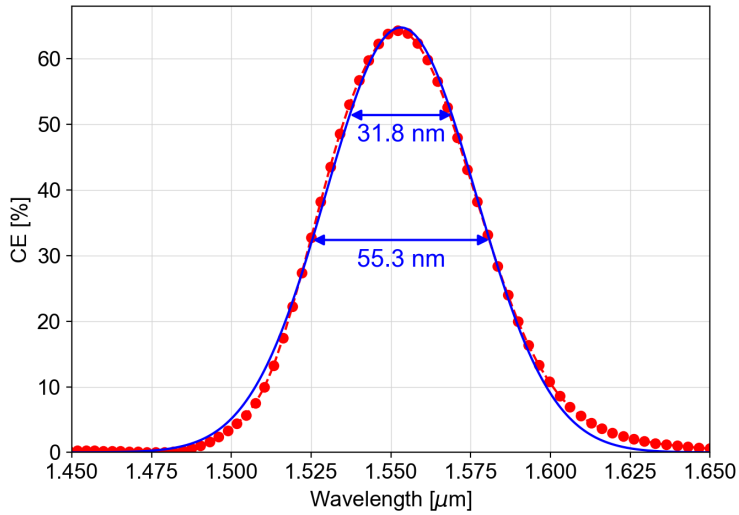

Figure 4.1: CE over wavelengths of (1550 ± 100) nm for the optimized apodized GC design, fitted with a gaussian function. Adapted from [34].

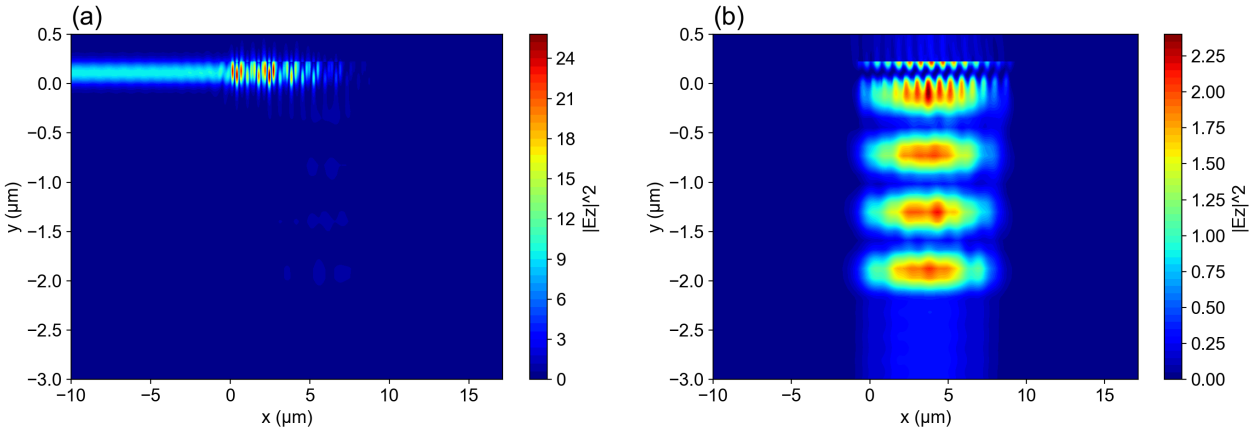

Figure 4.2: E-Field cross-sectional x-z-view of the in-coupling GC for a wavelength of **(a)** l550nm and **(b)** 1700nm.

strate the grating coupler's optimized performance at the target wavelength of 1550 nm and at the emission angle of 10°. As the grating coupler is designed for equal efficiency in both in-coupling and out-coupling, the focus will be on the grating coupler's in-coupling performance from here on.

4.2 Varying the Coupling Angle

This section presents the results of the linear approximation design for the grating coupler, optimized for an 8° coupling angle. As discussed in Section 3.2, the linear approximation simplifies the grating structure by keeping the grating period constant. To verify the behavior predicted by the Bragg condition (see Equation 2.2.6), a sweep over the grating period was performed using a series of 2D-FDTD simulations. The resulting transmission heatmap is shown in Figure 4.4(a). The results confirm the expected linear relationship between the grating period and the peak transmission wavelength. Specifically, as the grating period increases, the peak transmission shifts toward longer wavelengths. Additionally, smaller grating periods result

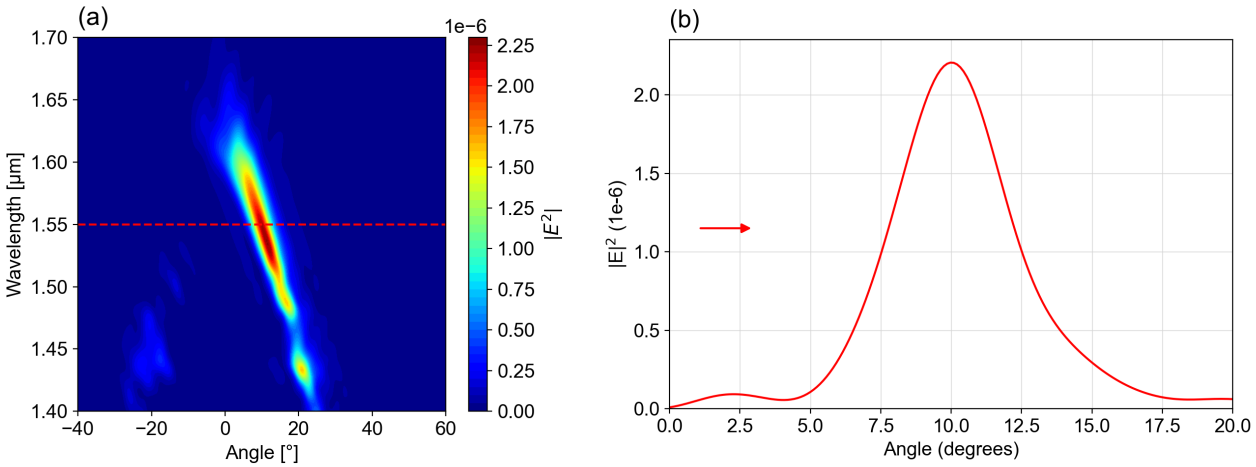

Figure 4.3: **(a)** Farfield projection of the outcoupling GC design, 1550 nm profile marked with a red dashed line. **(b)** Farfield projection profile at 1550 nm.

in lower peak transmission. This reduction can be attributed to weaker diffraction effects when the grating period becomes significantly smaller than the central wavelength, causing the light to propagate through the structure as though it were a uniform medium (see Chapter 2).

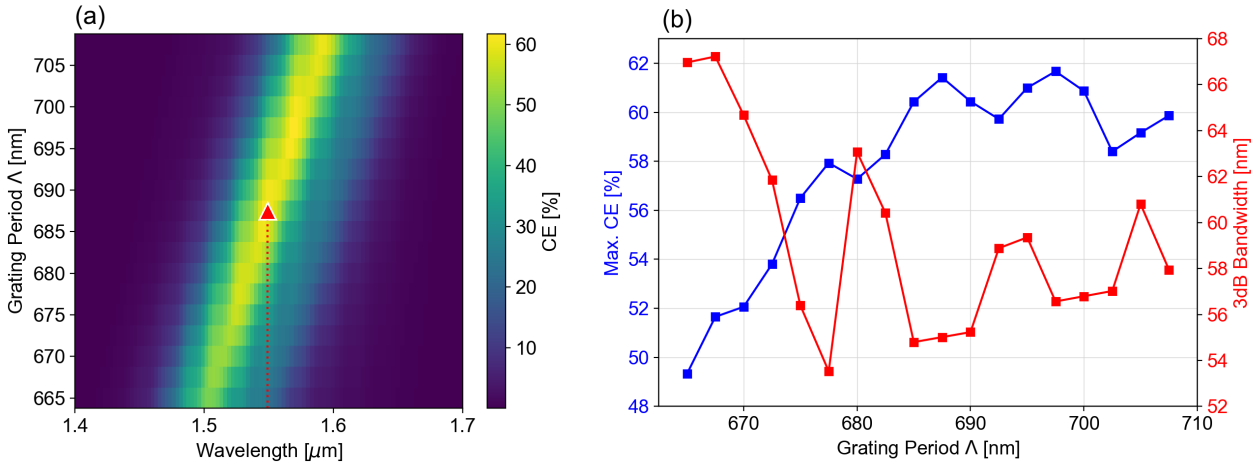

Figure 4.4: **(a)** Transmission heatmap depicting the grating period as a function of wavelength and transmission intensity. The highest CE at 1550 nm (red triangle) was found at a grating period of $\Lambda = 687.5$ nm. **(b)** Maximum CE and 3 dB bandwidth as functions of grating period Λ.

Figure 4.4(b) shows the relationship between the maximum CE and the 3-dB bandwidth for different grating periods. A higher peak CE corresponds to a narrower bandwidth, while a broader bandwidth leads to a lower peak CE. This inverse relationship can be attributed to the Gaussian field profile, where a higher peak results in a smaller bandwidth, and vice versa. However, neither the CE nor the bandwidth varies in a perfectly linear manner with respect to the grating period, as fluctuations are observed. These fluctuations are due to the emission spectra not following a typical Gaussian shape, as illustrated by the CE spectrum for $\Lambda = 687.5$ nm in Figure 4.5. Other linearly approximated designs exhibit similar non-Gaussian behavior. This deviation arises because the linear approximation does not account for the exact apodization profile, which causes the grating-diffracted field to not fully match a Gaussian field

distribution.

For the linearly approximated design, the grating period yielding the highest CE at 1550 nm was found to be $\Lambda = 687.5$ nm, resulting in a CE of 61.4% with a 3dB bandwidth of 55 nm. This result is highlighted by the red triangle in Figure 4.4(a). The result is only marginally lower than the theoretical value of 61.9% reported by [34] and the simulated value of 64.18% from Section 4.1 for a 10° coupling angle. Although the bandwidth is only 0.3 nm smaller than that of the initial optimized design, the deviation from the Gaussian profile suggests that bandwidth fluctuations may be more pronounced in experimental scenarios, where the field distribution is less controlled.

A uniform grating structure was also simulated for comparison. In this case, the grating gap widths w_i were kept constant across all gratings, calculated as:

$$w = \frac{\sum_i w_i}{24} = 139.6\,\text{nm}. \tag{4.2.1}$$

For the uniform design, the maximum CE at 1550 nm was found to be 45.37% with a grating period of $\Lambda = 696.19$ nm. This lower efficiency suggests that uniform grating structures are less effective for optimization purposes. A comparison of the CE spectra for the optimized apodized, linearly approximated, and uniform grating structures is shown in Figure 4.5.

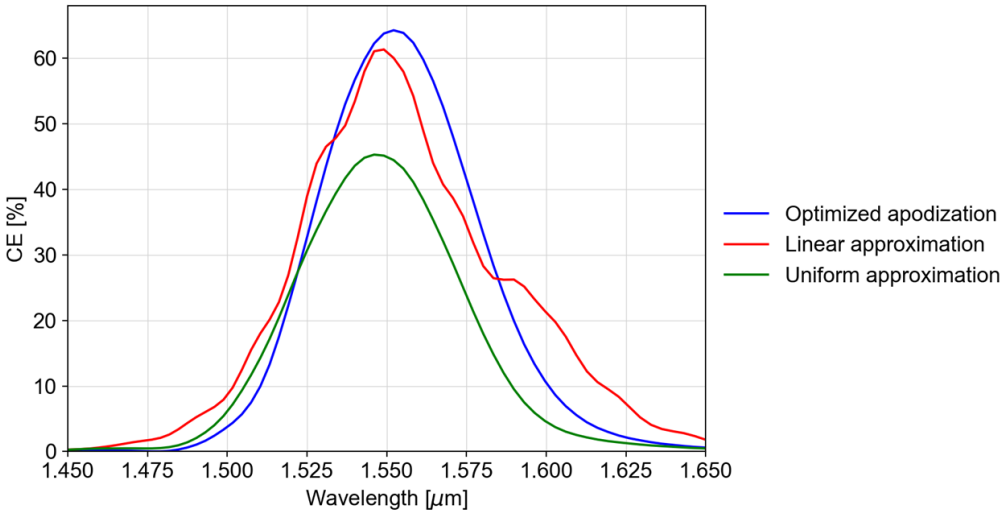

Figure 4.5: CE as a function of wavelength for different GC structures. The structures are listed in order of highest to lowest efficiency at 1550 nm: **(1)** Optimized apodized structure [34] (blue), 64.18% at 10° incidence; **(2)** Linearly approximated structure (red), 61.4% at 8° incidence; **(3)** Uniform structure (green), 45.37% at 10° incidence.

All in all, these results demonstrate that the linearly approximated design for an 8° coupling angle achieves a CE and bandwidth comparable to the optimized apodized grating design for a 10° coupling angle, while simplifying fabrication. As a result, the linear approximation has been established as a viable approach for high-efficiency 1D grating coupler designs. To further optimize the grating coupler, three-dimensional refinements must be explored. This is discussed in the next section.

4.3 Grating Width

The objective of this study was to determine the grating width that maximizes CE at a wavelength of 1550 nm. A parameter sweep of grating widths from 3 to 20 microns was conducted for both the optimized apodized GC design and its linear approximation using 3D-FDTD simulations.

The results of the sweep, presented in Figure 4.6, show that the CE increases as the grating width approaches the MFD of 10.4 μm, peaking at 11 μm. Beyond this point, the CE does not increase, indicating that a wider grating width does not significantly improve the efficiency. The optimized apodized grating coupler achieves a maximum CE of 60% at a width of 11 μm, while the linear approximation of this design exhibits a lower peak CE of 52.8% at the same width. The comparison of the two designs show that while the linear approximation exhibits a similar trend, it demonstrates a reduction in overall efficiency by approximately 7.3%. This deviation is notably larger than the margin observed in the previous findings discussed in Section 4.2. It is also worth noting that the maximum CE obtained from the 3D-FDTD simulations is lower than that observed in 2D-FDTD simulations. This discrepancy arises due to the inherent limitations of 2D-FDTD simulations, which neglect out-of-plane effects such as scattering and propagation losses in the third dimension.

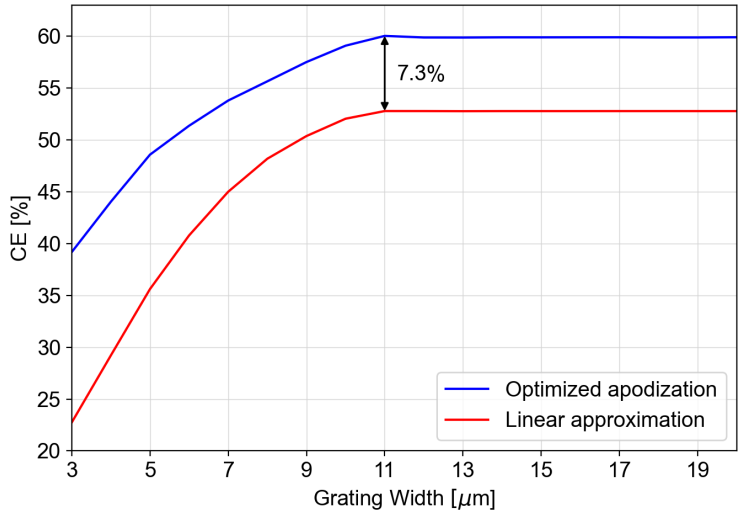

Figure 4.6: CE as a function of grating width at a wavelength of 1550 nm for an optimized apodized GC (blue) and its linear approximation (red).

In the FDTD simulations conducted here and in the previous section, the fiber-to-grating distance was set to 1 μm. No significant out-of-plane focusing effects were observed, indicating that high coupling efficiency can be achieved by positioning the fiber as close to the grating as possible. If the fiber were placed further from the grating, the Gaussian beam would expand and defocus, making wider gratings necessary to improve alignment tolerance and reduce sensitivity to small misalignments in practical experiments. However, increasing the grating width also introduces trade-offs: a wider grating may require a longer taper to efficiently transition into the narrower waveguide, thus increasing the device footprint. Consequently, the grating width of 12 μm was selected as the starting point for further analysis. The balance between grating width, taper length, and overall footprint must be carefully chosen in device design and is further explored in the next section on taper geometry optimization.

4.4 Taper Geometry

In this section, the taper geometry was analyzed with the key constraints being the input and output widths as well as the height of the waveguide. The height of the slab is chosen to be 220 nm, matching the height of the grating coupler. The input width, or taper width as we define it here, corresponds to the previously discussed grating width of 12 μm, and the output width matches that of the waveguide, which is 600 nm wide. The choice of the 600 nm waveguide width can be justified by the relationship between the effective index n_{eff} and the waveguide width, ensuring operation far from cut-off and avoiding higher-order modes, as shown in Figure 4.7.

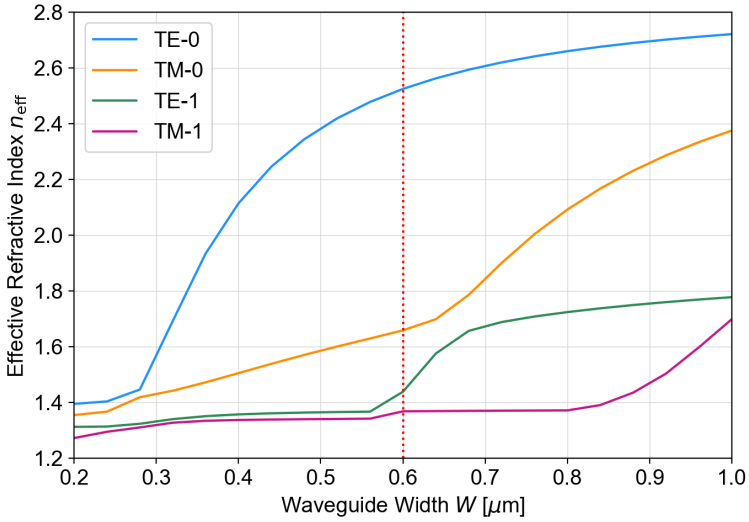

Figure 4.7: Effective refractive index n_{eff} as a function of the waveguide width for different modes. The 600 nm width is marked with a red dotted line.

Taper Length Sweep

To optimize the taper length, a linear taper was simulated with EME simulations, as presented in Section 3.3.2. A sweep over taper length for a fixed input width of 12 μm shows that transmission increases with taper length, as presented on the left in Figure 4.8. The results exhibit exponential convergence toward near 100% transmission, with low transmission at shorter lengths and near-complete transmission at a length of 300 μm. The taper length required to achieve over 98% transmission can be estimated theoretically using Equation 2.2.7 and Equation 2.2.8:

$$\theta_{\text{angle}} = 1.4 \cdot \frac{1550\text{nm}}{2 \cdot (12 - 0.6)\mu\text{m} \cdot 2.78} \approx 0.0342 \text{ rad},$$

$$\Rightarrow L = \frac{(12 - 0.6)\mu\text{m}}{2 \tan \theta_{\text{angle}}} \approx 166.4 \ \mu\text{m},$$

where the effective refractive index $n_{\text{eff}} \approx 2.78$ was determined from EME Solver calculations. Although the simulation results show that 98% transmission occurs at a taper length of approximately 200 μm (red triangle in Figure 4.8(left)), which is longer than the theoretical prediction of 166.4 μm, this discrepancy can be attributed to the fact that the analytical solution provides an indicative value, while the simulation accounts for additional effects not captured by the simplified calculation. Therefore, the analytical solution serves as a good approximation, but more precise results are obtained from the simulation.

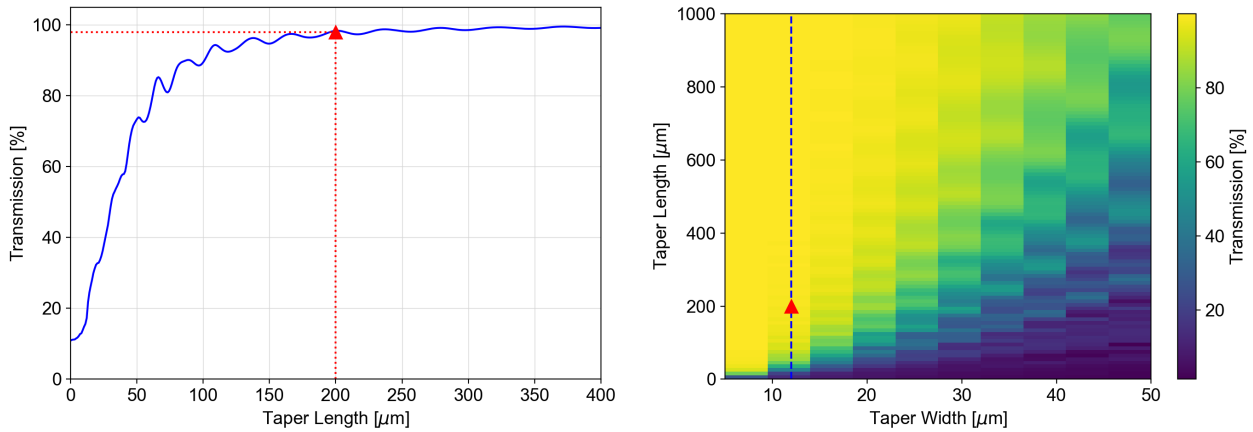

Figure 4.8: **Left:** Transmission efficiency vs. taper length for a fixed input width of 12 μm. The red triangle marks 98% transmission at 200 μm. **Right:** Heatmap of transmission as a function of taper width and length. The blue dashed line marks the taper with 12 μm width and 200 μm length plotted on the left.

In addition, a combined sweep of taper width and length was performed to investigate how transmission is affected under varying widths. This analysis is important for practical applications where precise alignment for grating couplers with small widths may be challenging. The right-hand side in Figure 4.8 shows the relationship between transmission efficiency, taper width, and taper length. The results demonstrate that higher transmission for wider taper widths requires longer taper lengths. This reveals a trade-off between ease of alignment and taper length: wider tapers are easier to align experimentally but require more physical space to achieve efficient mode transition and minimize propagation loss. As taper length increases, the overall device footprint grows, which can limit the compactness of the design. Therefore, the objective is to minimize the taper length while maintaining high transmission efficiency, optimizing the taper geometry for both efficient light coupling and a reduced footprint.

Taper Shape Sweep

The next consideration is whether modifying the taper shape can reduce the taper length while maintaining minimal losses. One approach is to explore different values for the exponent m in the parameterization of the taper design, as described in Equation 2.2.12, and analyze the impact of these shapes on taper performance. For this study, a taper length of 100 μm was selected, which allowed only 90% transmission in the case of a linear taper.

The results of the sweep are plotted in Figure 4.9, illustrating the effect of varying the exponent from 0.25 to 4. Notably, peak transmission occurs around an exponent of 1.75, suggesting that a near-parabolic taper is optimal for this length. A more detailed sweep within a narrower range identified the optimal exponent to be approximately 1.8, with deviations (e.g., between 1.4 and 1.9) resulting in significant fluctuation in transmission. The maximum transmission achieved with different taper shapes is capped at approximately 95%, which remains lower than the 98% transmission observed with a linear taper of 200 μm. Although the parabolic taper with an exponent of approximately 1.8 exhibits better performance than the linear taper at the same shorter 100 μm length, the fluctuations in transmission and the limited peak transmission do not justify the increased complexity in fabrication. While extending a parabolic taper could improve transmission, this would result in a length comparable to the 200 μm linear taper, eliminating the advantage of the shorter length. As a result, the linear taper remains the preferred design in this work due to its simplicity and stability.

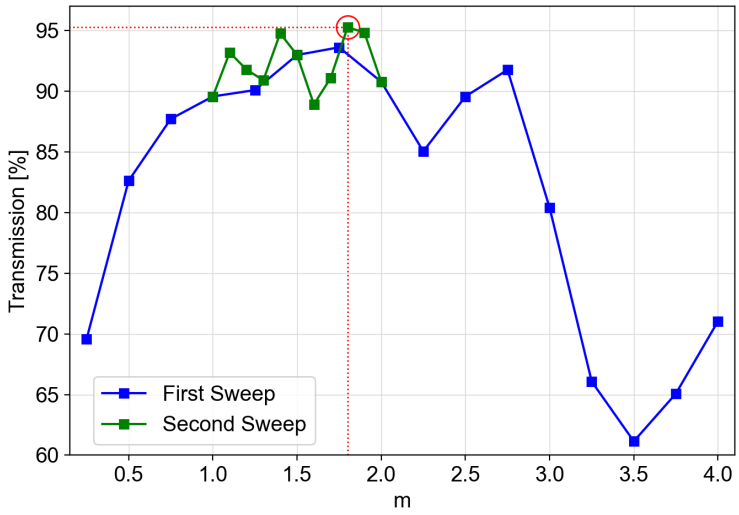

Figure 4.9: Transmission as a function of the taper shape parameter m for a taper length of 100 μm, with data from two parameter sweeps. The maximum transmission achieved of 95% is marked with a red circle at $m = 1.8$.

4.5 Simulation of a complete grating coupler design

Building upon the results from Section 4.3 and 4.4, a complete grating coupler structure was simulated using 3D-FDTD simulations. The optimized design incorporates a grating width of 12 μm and a taper length of 200 μm, as previously determined. This section aims to evaluate the full performance of the grating coupler, specifically focusing on the CE and bandwidth at the target wavelength of 1550 nm.

The simulation of the optimized apodized design with a 10° coupling angle at a single wavelength around 1550nm shows that the chosen taper leads to a 56% CE into the waveguide mode. The 3D results thus demonstrate a lower coupling efficiency, which was expected due to the added complexity in the 3D model, such as the taper section. The electric field distribution of this simulation is shown in Figure 4.10, where the field is visualized across a cross-sectional view of the GC. The taper region extends from -200 to 0 μm along the x-direction, and the grating begins at 0μm, as marked in the figure. It can be observed that the light is effectively coupled and confined within the waveguide, highlighting the role of the taper in guiding the light into the narrower waveguide. Additionally, almost no absorption in the substrate can be seen, similarly to the 2D-FDTD simulation done in Section 4.2, Figure 4.2(a).

Next, the design was evaluated over a broader wavelength range (1.5 to 1.6 μm). The performance remained consistent, with a CE of 59.3% at 1550 nm and a 3dB bandwidth of 57.1 nm, as shown in the blue curve of Figure 4.11. Similarly, the linear approximated design with the optimal grating period found in Section 4.2 was simulated over the same wavelength range, see the red curve in Figure 4.11. This design achieved a lower CE at 1550 nm of 47.8%, albeit with a larger BW of 67.3nm around the peak wavelength of 1552 nm. The comparison between the two designs demonstrates that coupling efficiencies of 50% or higher are achievable for both configurations. While the 8° linear approximated design exhibits a slightly lower CE at 1550 nm, its broader bandwidth and simpler fabrication process, due to the constant grating period, make it less sensitive to fabrication errors. This trade-off in efficiency can be considered favorable in other practical applications.

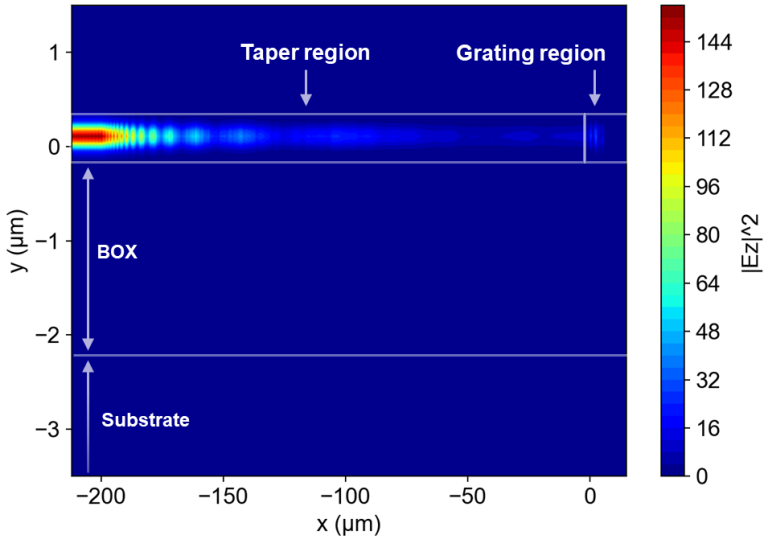

Figure 4.10: Electric field distribution in the 3D-FDTD simulation of the optimized apodized GC, showing the propagation of light from the grating region to the taper region.

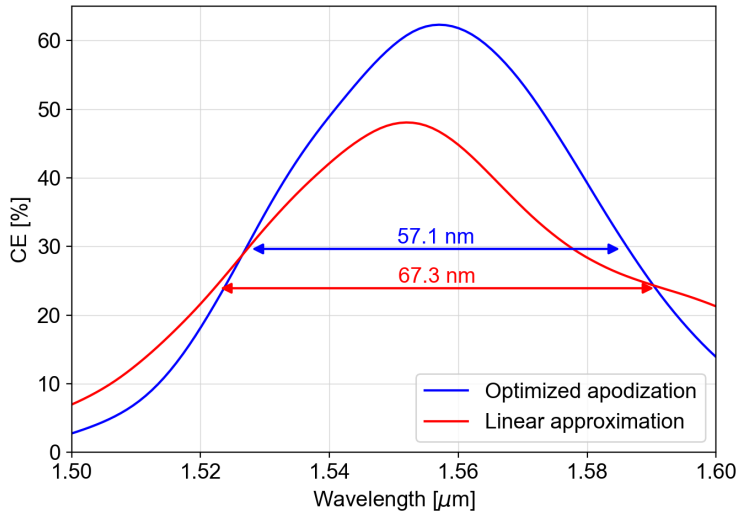

Figure 4.11: CE as a function of wavelength for the optimized apodized grating coupler (10°) and the linear approximation design (8°) in 3D-FDTD simulations.

Conclusion

By systematically optimizing the grating and taper structures, this work successfully realized a high-efficiency SOI grating coupler that meets the experimental requirements. Starting with a CE of 65% and a 55 nm 3 dB BW in the initial apodized design using 2D-FDTD simulations at a 10° angle, the analysis was completed in 3D-FDTD simulations, yielding a CE of 59% and a 3 dB BW of 57 nm. Despite a lower CE at 1550 nm in the final simulations, the peak CE at 1557 nm still reached 63%, nearly matching the initial 2D-simulated value. The shift in central wavelength is likely due to the increased mesh size used in the 3D simulations. This adjustment was necessary to manage the computational load introduced by the added dimension. A coarser mesh can affect the accuracy of the effective refractive index calculation, which in turn influences the central wavelength of the GC. Overall, the achieved CE meets

the target value of 50%, with a bandwidth that is broader than most AGCs demonstrated in literature, as shown in Table 1.1.

The linear approximated design demonstrated a lower CE of 48% at 1550 nm with a 3dB BW of 67 nm. The simulations showed that the CE dropped by nearly 9% when transitioning to 3D and by another 5% when incorporating the taper structure. This decrease is likely attributed to the linear approximation of the apodization profile, which does not perfectly match the Gaussian-like field distribution of the fiber. Consequently, this mismatch leads to unpredictable light propagation behavior in the added dimension, suggesting that the linear approximation may not sufficiently capture the complexity of the apodization. A potential improvement could involve adopting a different parameterization of the apodization profile to better accommodate the fiber's field distribution and adapt to the varying incident angles. Although the linearly approximated design did not fully meet the 50% CE target, the broader BW is highly advantageous for the intended applications of this grating coupler.

It is also plausible that the optimized apodized design, which achieved 59% CE, could perform well at an 8° angle in a practical setup, potentially eliminating the need for the linearly approximated design. Nevertheless, experimental validation will be crucial to confirm these simulation results, as fabrication errors and setup misalignments often cause deviations in realistic performance. The next section will present the chip design intended for experimental validation and outline the future steps based on the findings of this study.

Chapter 5

Outlook

The 3D GC design developed in this work establishes a solid foundation, validated through extensive simulations with optimized parameters for both the grating and taper sections. This chapter proposes a chip design in ***Section 5.1****, followed by a discussion in* ***Section 5.2*** *on potential areas for improvement and research directions to further enhance the design and performance of the grating coupler. These insights will guide the continuation of this work in the upcoming future.*

5.1 Chip design

The next immediate step is to fabricate and measure a chip with the simulated GC structures. Figure 5.1 shows the pattern design of the SOI chip, which will be used for experimental validation of my results. The pattern has a size of 12.8×12.8 mm^2, which can well fit onto a 15×15 mm^2 chip, a standard size used in our nanofabrication facility for prototyping. This chip includes parameter sweeps for the grating coupler, taper geometry, and ring resonator configurations to further optimize the performance and explore any deviations between experimental data and theoretical predictions. All GCs are placed at a pitch of 254 μm from each other to account for the 127 μm distance between the SMFs.

The chip is divided into four distinct sections (**A**, **B**, **C**, and **D** in Figure 5.1), each designed to evaluate different aspects of grating coupler performance. Section **A** focuses on verifying the 10-degree apodized design by testing a column of gratings with a fixed width of 30 μm, which eases alignment. The taper length is varied from 50 to 530 μm in 30 μm increments. This setup explores how the 8° fiber angle affects a design originally optimized for a 10° angle, providing insights into its flexibility. According to the results from Section 4.4, high CE values are expected at longer taper lengths, though shorter tapers are also considered for their potential bandwidth advantages and reduced footprint.

Section **B** investigates the linear approximated design. Here, the grating period is swept from 680.5 nm to 696 nm in 0.5-nm increments, while maintaining a fixed 8° coupling angle, a taper length of 200 μm, and a grating width of 25 μm. This sweep aims to confirm the linear relationship predicted by the Bragg condition, as demonstrated in Section 4.2 and visualized in Figure 4.4(a). The GCs are arranged in two rows, with the second row offset by half the sweep increment. This allows for finer tuning and comparison during subsequent measurements.

Section **C** continues to explore the linear approximated design but fixes the grating period at Λ = 687.5 nm, as determined from 2D- and 3D-FDTD simulations to be optimal for a wavelength of 1550 nm. The taper width is swept from 12 to 40 μm in 2 μm increments, while the taper length is varied as in Section A. This section aims to identify the optimal GC structure

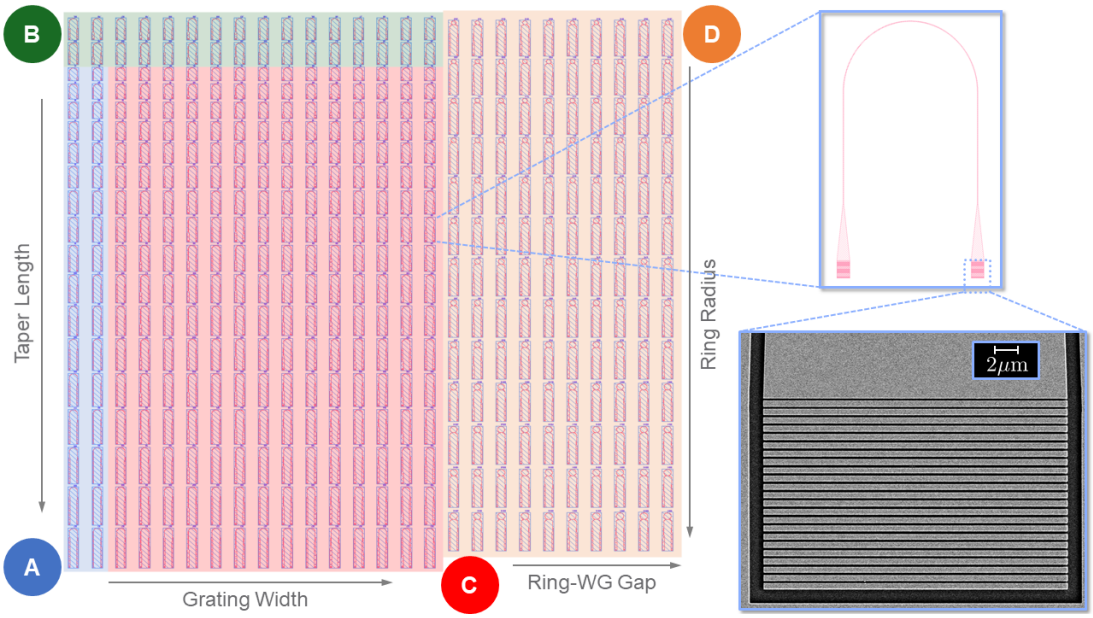

Figure 5.1: Photonic SOI chip design with four sections (A-D), each testing various grating coupler and ring resonator parameters. Arrows indicate the directions of parameter sweeps. The insets on the right provide a close-up of a GC design and a SEM image of the fabricated grating structure.

for maximizing coupling efficiency while maintaining a broad bandwidth, to be compared with the results presented in Section 4.5.

In Section **D**, ring resonators are integrated alongside the linear approximated apodized grating coupler, using the same grating period as in Section C. The taper length is fixed at 400 μm, and the grating width is set at 25 μm, which should allow for CE above 50% according to the simulated results in Section 4.3 and 4.4. Here, the gap between the resonator and the waveguide is varied from 0.1 to 1 μm in 0.1 μm increments, while the ring radius is swept from 36 to 60 μm in 2 μm steps. This setup aims to characterize the effective indices and propagation losses, providing insight into how the waveguide bend influences light propagation and coupling performance.

It is anticipated that experimental results will differ from simulations due to fabrication constraints. For example, the BOX thickness used in the simulations was set at 2.2 μm, whereas in fabrication it is 2 μm thick. This discrepancy could influence the directionality of the grating coupler and reduce the coupling efficiency [37]. Fabrication imperfections, such as errors during the etching process or the addition of the cladding, could also impact performance, although the scanning electron microscope (SEM) image of the fabricated grating structure (Figure 5.1) indicates promising accuracy in grating patterning.

5.2 Next steps

While this work has demonstrated promising results, some aspects of the GC design could be refined in the future to achieve even better performance.

In many AGCs presented in literature, including those built on in this work, the constant grating period does not fully satisfy the Bragg condition across all scattering elements. This is due to variations in the fill factor that cause the effective refractive index n_{eff} to change along the grating length, leading to the Bragg condition being met at only one specific point. Recent

advances in simultaneous apodization of both the fill factor and grating period, as demonstrated in [33, 39], offer avenues for more accurately satisfying the Bragg condition along the entire grating, which could lead to higher CE and broader bandwidth. Additionally, optimization techniques such as genetic algorithms and machine learning could be leveraged to refine the grating apodization further, pushing the performance beyond current benchmarks. The taper shape, which was partially addressed in this work, can also be further optimized through these approaches.

Though this thesis was based on specific initial conditions, the methodologies used in this work can be adapted to different conditions. For instance, [37] showed that BOX thickness significantly affects coupling, making it an important factor in future research. Exploration of thicker silicon stack-ups, as demonstrated in [34], also holds promise for improving the coupling efficiency. Building on the foundation laid by this study, future work can push the limits of grating coupler performance while exploring innovative solutions for improved scalability and efficiency.

Chapter 6

Conclusion

This work presented the design and simulation of a high-efficiency grating coupler for SOI platforms within the set initial conditions. First, I recreated an optimized apodized GC taken from literature as a starting point through 2D-FDTD Simulations. Based on this design, I explored a linear approximation strategy to accomodate the grating structure for a different coupling angle without sacrificing much of the peak CE. The study was then extended to 3D-FDTD simulations, where I investigated variations in grating width. Additionally, I took the taper geometry into account by exploring the taper length and shape parameters with the use of EME simulations. By accomodating the initial design to our experimental constraints and exploring the previously under-investigated aspects of engineering the grating's lateral size and the tapering of the coupling section to seamlessly match the waveguide width, a complete GC design was finalized that balances high coupling efficiency with practical considerations for alignment and fabrication. The optimized parameters yielded GCs with a CE at 1550nm of approximately 60% and 48% and a 3 dB BW of 57 nm and 67 nm for the initial apodized and linear approximated design, respectively. Consequently, the results indicate good performance for different applicational fields.

The next phase of this research involves fabricating and testing the proposed GC designs. Measurements on the chip discussed in Chapter 5 will enable a comparison between real-world performance and the simulated results, with a focus on confirming the coupling efficiency and bandwidth under practical conditions.

In the broader context of integrated photonics, this work contributes to the development of scalable and efficient grating couplers for silicon photonics. By achieving high performance without the need for additional back reflectors, the proposed design reduces fabrication complexity and cost. This streamlined approach demonstrates that efficient couplers can be integrated into photonic circuits with fewer processing steps, while maintaining excellent performance. As silicon photonics continues to evolve, the ability to manufacture cost-effective, high-efficiency couplers will be essential in advancing applications in data communications, quantum computing, and other emerging fields.

This page is left intentionally blank

Acknowledgements

I would like to extend my deepest gratitude to the following people, without whom the completion of this thesis would not have been possible.

First and foremost, I want to thank Prof. Dr. Wolfram Pernice for giving me the opportunity to work on this project and for providing the necessary framework and support throughout the process.

I am especially grateful to my supervisor, Dr. Simone Ferrari, who guided me through this thesis from start to finish and always made sure to take time for me despite his busy schedule.

Furthermore, I would like to thank Prof. Dr. Lauriane Chomaz for agreeing to serve as the second examiner of my thesis, despite the short notice.

I would also like to express my gratitude to Ravi Pradip, whose guidance was invaluable in addressing my numerous questions and technical inquiries.

A special thanks I would like to extend to Liam McRae for helping me get started with Lumerical and troubleshoot issues in my code, Qinlin Zhang for assisting me with gdshelpers, and Kilian Welz for fabricating the chip and taking the SEM images.

At large, I would like to acknowledge the entire AG Pernice group for creating a welcoming and collaborative atmosphere that made my time in the office enjoyable.

Finally, I would like to thank my family for always being there for me. Especially my mom, who always makes sure I have a warm meal on the table and my sister, who has been my biggest emotional support not just for the duration of this thesis, but throughout my entire life.

List of Abbreviations

Abbreviation	Meaning
AGC	Apodized Grating Coupler
BC	Boundary Condition
BOX	Buried Oxide
BW	Bandwidth
CE	Coupling Efficiency
CMOS	Complementary Metal-Oxide Semiconductor
EME	Eigenmode Expansion
FDTD	Finite-Difference Time-Domain
FF	Fill Factor
GA	Genetic Algorithm
GC	Grating Coupler
GP	Grating Period
MFD	Mode Field Diameter
PICs	Photonic Integrated Circuits
PML	Perfectly Matched Layer
SEM	Scanning electron microscope
SMF	Single-Mode Fiber
SNSPD	Superconducting Nanowire Single-Photon Detector
SOI	Silicon-On-Insulator
TE-MODE	Transverse Electric Mode
TM-MODE	Transverse Magnetic Mode
UGC	Uniform Grating Coupler
WG	Waveguide

Bibliography

[1] A. V. Krishnamoorthy, K. W. Goossen, W. Jan, X. Zheng, R. Ho, G. Li, R. Rozier, F. Liu, D. Patil, J. Lexau, H. Schwetman, D. Feng, M. Asghari, T. Pinguet, and J. E. Cunningham, "Progress in low-power switched optical interconnects," IEEE Journal of Selected Topics in Quantum Electronics, vol. 17, no. 2, pp. 357–376, 2011.

[2] R. G. Hunsperger, Photonic Integrated Circuits, 6th ed. New York: Springer, 2010.

[3] J. P. Dakin and R. Brown, Eds., Handbook of Optoelectronics: Concepts, Devices, and Techniques (Volume One), 2nd ed. CRC Press, 2017. https://doi.org/10.1201/9781315157009

[4] Y. Shi, Y. Zhang, Y. Wan, Y. Yu, Y. Zhang, X. Hu, X. Xiao, H. Xu, L. Zhang, and B. Pan, "Silicon photonics for high-capacity data communications," Photonics Research, vol. 10, pp. A106–A134, 2022. https://doi.org/10.1364/PRJ.446241

[5] H. H. Li, "Refractive index of silicon and germanium and its wavelength and temperature derivatives," Journal of Physical and Chemical Reference Data, vol. 9, no. 3, pp. 561–658, 1993.

[6] C. Z. Tan, "Determination of refractive index of silica glass for infrared wavelengths by ir spectroscopy," Journal of Non-Crystalline Solids, vol. 223, pp. 158–163, 1998.

[7] G. T. Reed and A. P. Knights, Silicon Photonics: An Introduction, 2nd ed. Wiley, 2019.

[8] J. Sun, E. Timurdogan, A. Yaacobi, Z. Su, E. S. Hosseini, D. B. Cole, G. Leake, A. R. Watts, and M. R. Watts, "Electronic band-gap modified passive silicon optical modulator at telecommunications wavelengths," Optics Express, vol. 23, no. 18, pp. 23 334–23 341, 2015.

[9] D. Thomson, A. Zilkie, J. E. Bowers, T. Komljenovic, G. T. Reed, L. Vivien, D. Marris-Morini, E. Cassan, L. Virot, J.-M. Fédéli, J.-M. Hartmann, J. H. Schmid, D.-X. Xu, F. Boeuf, P. O'Brien, G. Z. Mashanovich, and M. Nedeljkovic, "Roadmap on silicon photonics," Journal of Optics, vol. 18, p. 073003, 2016.

[10] B. Jalali and S. Fathpour, "Silicon photonics," Journal of Lightwave Technology, vol. 24, no. 12, pp. 4600–4615, 2006.

[11] S. Shekhar, W. Bogaerts, L. Chrostowski et al., "Roadmapping the next generation of silicon photonics," Nature Communications, vol. 15, p. 751, 2024. https://doi.org/10.1038/s41467-024-44750-0

[12] J. Wang, CMOS-Compatible Efficient Fiber-to-Chip Coupling. Singapore: Springer Singapore, 2019, pp. 173–194. https://doi.org/10.1007/978-981-13-3378-1_5

[13] H. Sunak, "Single-mode fiber measurements," IEEE Transactions on Instrumentation and Measurement, vol. 37, no. 4, pp. 557–560, 1988.

[14] G.-F. Cheng, Q. Yi, F. Xu, M. Yang, Z. Yan, Q. Li, Y. Zou, Y. Yu, and L. Shen, "Efficient 1.55 and 2μm Dual-Band SOI Grating Coupler for Light Coupling and On-Chip Wavelength Division (De)multiplexing," Advanced Photonics Research, vol. 4, 2023. https://api.semanticscholar.org/CorpusID:258195128

[15] X. Liu, Y. Zhao, H. Huang, Y. Li, X. She, H. Liao, J. Zhu, Z. Zhu, R. Huang, H. Liu, Z. Sheng, and F. Gan, "Compact, ultrabroadband and temperature-insensitive arbitrary ratio power splitter based on adiabatic rib waveguides," Applied Optics, vol. 62, no. 5, pp. 1279–1284, 2023. https://doi.org/10.1364/AO.479304

[16] D. Dai, L. Liu, S. Gao, D. Xu, and S. He, "Polarization management for silicon photonic integrated circuits," Laser & Photonics Reviews, vol. 7, May 2013.

[17] G. Son, S. Han, J. Park, K. Kwon, and K. Yu, "High-efficiency broadband light coupling between optical fibers and photonic integrated circuits," Nanophotonics, vol. 7, no. 12, pp. 1845–1864, 2018. https://doi.org/10.1515/nanoph-2018-0075

[18] R. Marchetti, C. Lacava, L. Carroll, K. Gradkowski, and P. Minzioni, "Coupling strategies for silicon photonics integrated chips," Photonics Research, vol. 7, no. 2, p. 201, 2019.

[19] X. Mu, S. Wu, L. Cheng, and H. Y. Fu, "Edge couplers in silicon photonic integrated circuits: A review," Applied Sciences, vol. 10, p. 1538, 2020. https://doi.org/10.3390/app10041538

[20] M. Pu, L. Liu, H. Ou, K. Yvind, and J. M. Hvam, "Ultra-low-loss inverted taper coupler for silicon-on-insulator ridge waveguide," Optics Communications, vol. 283, no. 19, pp. 3678–3682, 2010.

[21] T. Tekin, "Review of packaging of optoelectronic, photonic, and mems components," IEEE Journal of Selected Topics in Quantum Electronics, vol. 17, no. 3, pp. 704–719, 2011.

[22] L. Cheng, S. Mao, Z. Li, Y. Han, and H. Y. Fu, "Grating couplers on silicon photonics: Design principles, emerging trends and practical issues," Micromachines, vol. 11, 7 2020.

[23] S. Nambiar, P. Sethi, and S. Selvaraja, "Grating-assisted fiber to chip coupling for SOI photonic circuits," Applied Sciences, vol. 8, p. 1142, 2018. https://doi.org/10.3390/app8071142

[24] E. Lomonte, M. Stappers, L. Krämer, W. H. P. Pernice, and F. Lenzini, "Scalable and efficient grating couplers on low-index photonic platforms enabled by cryogenic deep silicon etching," 2023. https://arxiv.org/abs/2305.00907

[25] H. Gehring, A. Eich, C. Schuck, and W. H. P. Pernice, "Broadband out-of-plane coupling at visible wavelengths," Opt. Lett., vol. 44, no. 20, pp. 5089–5092, Oct 2019. https://opg.optica.org/ol/abstract.cfm?URI=ol-44-20-5089

[26] H. Gehring, M. Blaicher, W. Hartmann, P. Varytis, K. Busch, M. Wegener, and W. H. P. Pernice, "Low-loss fiber-to-chip couplers with ultrawide optical bandwidth," APL Photonics, vol. 4, no. 1, p. 010801, 01 2019. https://doi.org/10.1063/1.5064401

[27] D. Taillaert, F. V. Laere, M. Ayre, W. Bogaerts, D. V. Thourhout, P. Bienstman, and R. Baets, "Grating couplers for coupling between optical fibers and nanophotonic waveguides," Japanese Journal of Applied Physics, Part 1: Regular Papers and Short Notes and Review Papers, vol. 45, pp. 6071–6077, 8 2006.

[28] D. Vermeulen, S. Selvaraja, P. Verheyen, G. Lepage, W. Bogaerts, P. Absil, D. V. Thourhout, and G. Roelkens, "High-efficiency fiber-to-chip grating couplers realized using an advanced cmos-compatible silicon-on-insulator platform," Opt. Express, vol. 18, pp. 18 278–18 283, 2010.

[29] G. Roelkens, D. V. Thourhout, and R. Baets, "High efficiency silicon-on-insulator grating coupler based on a poly-silicon overlay," Opt. Express, vol. 14, pp. 11 622–11 630, 2006.

[30] S. Selvaraja, D. Vermeulen, M. Schaekers, E. Sleeckx, W. Bogaerts, G. Roelkens, P. Dumon, D. V. Thourhout, and R. Baets, "Highly efficient grating coupler between optical fiber and silicon photonic circuit," in Conference on Lasers and Electro-Optics (CLEO). Optical Society of America, 2009.

[31] F. V. Laere, T. Claes, J. Schrauwen, S. Scheerlinck, W. Bogaerts, D. Taillaert, L. O'Faolain, D. V. Thourhout, and R. Baets, "Compact focusing grating couplers for silicon-on-insulator integrated circuits," IEEE Photonics Technology Letters, vol. 19, no. 23, pp. 1919–1921, Dec 2007.

[32] N. Hoppe, W. S. Zaoui, L. Rathgeber, Y. Wang, R. H. Klenk, W. Vogel, M. Kaschel, S. L. Portalupi, J. Burghartz, and M. Berroth, "Ultra-efficient silicon-on-insulator grating couplers with backside metal mirrors," IEEE Journal of Selected Topics in Quantum Electronics, vol. 26, no. 2, pp. 1–6, 2020.

[33] V. Vitali, T. D. Bucio, C. Lacava, R. Marchetti, L. Mastronardi, T. Rutirawut, G. Churchill, J. Faneca, J. C. Gates, F. Gardes, and P. Petropoulos, "High-efficiency reflector-less dual-level silicon photonic grating coupler," Photonics Research, vol. 11, p. 1275, 7 2023.

[34] A. Bozzola, L. Carroll, D. Gerace, I. Cristiani, and L. C. Andreani, "Optimising apodized grating couplers in a pure SOI platform to −0.5 db coupling efficiency," Opt. Express, vol. 23, no. 12, pp. 16 289–16 304, Jun 2015. https://opg.optica.org/oe/abstract.cfm?URI=oe-23-12-16289

[35] M. H. Lee, J. Y. Jo, D. W. Kim, Y. Kim, and K. H. Kim, "Comparative study of uniform and nonuniform grating couplers for optimized fiber coupling to silicon waveguides," Journal of the Optical Society of Korea, vol. 20, no. 2, pp. 291–299, 2016. https://doi.org/10.3807/JOSK.2016.20.2.291

[36] D. Taillaert, P. Bienstman, and R. Baets, "Compact efficient broadband grating coupler for silicon-on-insulator waveguides," Opt. Lett., vol. 29, no. 23, pp. 2749–2751, Dec 2004. https://opg.optica.org/ol/abstract.cfm?URI=ol-29-23-2749

[37] M. Antelius, K. B. Gylfason, and H. Sohlstrom, "An apodized SOI waveguide-to-fiber surface grating coupler for single lithography silicon photonics," Optics Express, vol. 19, no. 4, pp. 3592–3598, 2011.

[38] J. Goh, I. Fushman, D. Englund, and J. Vučković, "Genetic optimization of photonic bandgap structures," Opt. Express, vol. 15, no. 13, pp. 8218–8230, Jun 2007. https://opg.optica.org/oe/abstract.cfm?URI=oe-15-13-8218

[39] R. Marchetti, C. Lacava, A. Khokhar, X. Chen, I. Cristiani, D. J. Richardson, G. T. Reed, P. Petropoulos, and P. Minzioni, "High-efficiency grating-couplers: Demonstration of a new design strategy," Scientific Reports, vol. 7, 12 2017.

[40] L. He, Y. Liu, C. Galland, A. E.-J. Lim, G.-Q. Lo, T. Baehr-Jones, and M. Hochberg, "A high-efficiency nonuniform grating coupler realized with 248-nm optical lithography," IEEE Photonics Technology Letters, vol. 25, no. 14, pp. 1358–1361, 2013.

[41] X. Chen, C. Li, and H. K. Tsang, "Fabrication-tolerant waveguide chirped grating coupler for coupling to a perfectly vertical optical fiber," IEEE Photonics Technology Letters, vol. 20, pp. 1914–1916, 2008.

[42] J. Schrauwen, F. Van Laere, D. Van Thourhout, and R. Baets, "Focused-ion-beam fabrication of slanted grating couplers in silicon-on-insulator waveguides," IEEE Photonics Technology Letters, vol. 19, no. 11, pp. 816–818, 2007.

[43] B. Wang, J. Jiang, and G. Nordin, "Embedded slanted grating for vertical coupling between fibers and silicon-on-insulator planar waveguides," IEEE Photonics Technology Letters, vol. 17, no. 9, pp. 1884–1886, 2005.

[44] W. S. Zaoui, A. Kunze, W. Vogel, M. Berroth, J. Butschke, F. Letzkus, and J. Burghartz, "Bridging the gap between optical fibers and silicon photonic integrated circuits," Optics Express, vol. 22, no. 2, p. 1277, 2014.

[45] Y. Ding, H. Ou, and C. Peucheret, "Ultrahigh-efficiency apodized grating coupler using fully etched photonic crystals," Opt. Lett., vol. 38, no. 15, pp. 2732–2734, Aug 2013. https://opg.optica.org/ol/abstract.cfm?URI=ol-38-15-2732

[46] Y. Ding, C. Peucheret, H. Ou, and K. Yvind, "Fully etched apodized grating coupler on the SOI platform with −0.58 dB coupling efficiency," Opt. Lett., vol. 39, no. 18, pp. 5348–5350, Sep 2014. https://opg.optica.org/ol/abstract.cfm?URI=ol-39-18-5348

[47] M. Passoni, D. Gerace, L. Carroll, and L. C. Andreani, "Grating couplers in silicon-on-insulator: The role of photonic guided resonances on lineshape and bandwidth," Applied Physics Letters, vol. 110, no. 4, p. 041107, 2017. https://doi.org/10.1063/1.4974992

[48] W. D. Sacher, Y. Huang, L. Ding, B. J. F. Taylor, H. Jayatilleka, G.-Q. Lo, and J. K. S. Poon, "Wide bandwidth and high coupling efficiency Si3N4-on-SOI dual-level grating coupler," Opt. Express, vol. 22, no. 9, pp. 10 938–10 947, May 2014. https://opg.optica.org/oe/abstract.cfm?URI=oe-22-9-10938

[49] M. Zhang, H. Liu, B. Wang, G. Li, and L. Zhang, "Efficient grating couplers for space division multiplexing applications," IEEE Journal of Selected Topics in Quantum Electronics, vol. 24, no. 6, pp. 1–5, 2018.

[50] X. Chen and H. K. Tsang, "Polarization-independent grating couplers for silicon-on-insulator nanophotonic waveguides," Opt. Lett., vol. 36, no. 6, pp. 796–798, Mar 2011. https://opg.optica.org/ol/abstract.cfm?URI=ol-36-6-796

[51] J. Münzberg, A. Vetter, F. Beutel, W. Hartmann, S. Ferrari, W. H. P. Pernice, and C. Rockstuhl, "Superconducting nanowire single-photon detector implemented in a 2D photonic crystal cavity," Optica, vol. 5, no. 5, pp. 658–665, May 2018. https://opg.optica.org/optica/abstract.cfm?URI=optica-5-5-658

[52] S. Ferrari, C. Schuck, and W. Pernice, "Waveguide-integrated superconducting nanowire single-photon detectors," Nanophotonics, vol. 7, no. 11, pp. 1725–1758, 2018. https://doi.org/10.1515/nanoph-2018-0059

[53] DARPA, "Nanowatt platforms for sensing, analysis, and computation," n.d., accessed: September 12, 2024. https://www.darpa.mil/program/nanowatt-platforms-for-sensing-analysis-and-computation

[54] R. O. Jr. and X. Meng, Principles of Photonic Integrated Circuit. Berlin, Heidelberg: Springer, 2021.

[55] S. A. Abazi, "Integrated nano-photonic devices for non-linear optics-based single-photon sources," Master's thesis, University of Münster, November 2019, first Supervisor: Jun. Prof. Dr. Carsten Schuck, Second Supervisor: Prof. Dr. Wolfram Pernice.

[56] D. J. Griffiths, Introduction to Electrodynamics, 4th ed. Cambridge: Cambridge University Press, 2021.

[57] A. Hebecker, "Lecture notes on theoretical physics III," 2023, https://www.thphys.uni-heidelberg.de/~hebecker/TP3/notes.pdf.

[58] G. Lifante, Integrated Photonics: Fundamentals, 1st ed. Wiley, Jan. 2003. https://onlinelibrary.wiley.com/doi/book/10.1002/0470861401

[59] E. Hecht, Optics. Addison-Wesley, 2002.

[60] L. Chrostowski and M. Hochberg, Silicon Photonics Design: From Devices to Systems. Cambridge: Cambridge University Press, 2015.

[61] Y. Fu, T. Ye, W. Tang, and T. Chu, "Efficient adiabatic silicon-on-insulator waveguide taper," Photonics Research, vol. 2, p. A41, 6 2014.

[62] F. Olyslager, Electromagnetic waveguides and transmission lines. OUP Oxford, 1999, vol. 51.

[63] V. Muniswamy and N. Krishnaswamy, "Modelling, design and optimization of compact taper and gratings for mode coupling to SOI waveguides at C-band," Journal of Modern Optics, vol. 67, pp. 1112–1119, 7 2020.

[64] C. R. Doerr, L. Chen, Y.-K. Chen, and L. L. Buhl, "Wide bandwidth silicon nitride grating coupler," IEEE Photonics Technology Letters, vol. 22, no. 19, pp. 1461–1463, 2010.

[65] Z. Xiao, F. Luan, T.-Y. Liow, J. Zhang, and P. Shum, "Design for broadband high-efficiency grating couplers," Opt. Lett., vol. 37, no. 4, pp. 530–532, Feb 2012. https://opg.optica.org/ol/abstract.cfm?URI=ol-37-4-530

[66] E. Lomonte, F. Lenzini, and W. H. P. Pernice, "Efficient self-imaging grating couplers on a lithium-niobate-on-insulator platform at near-visible and telecom wavelengths," Optics Express, vol. 29, p. 20205, 6 2021.

[67] Ansys, Inc., "MODE - EigenMode Expansion (EME) Solver Introduction," accessed: August 12, 2024. https://optics.ansys.com/hc/en-us/articles/360034396614-MODE-EigenMode-Expansion-EME-solver-introduction

[68] ——, "Finite Difference Time Domain (FDTD) solver introduction," accessed: September 5, 2024. https://optics.ansys.com/hc/en-us/articles/360034914633-Finite-Difference-Time-Domain-FDTD-solver-introduction

[69] J. Petracek and J. Luksch, "Bidirectional eigenmode propagation algorithm for 3D waveguide structures," International Conference on Transparent Optical Networks, pp. 1–4, June 2011.

[70] D. F. G. Gallagher and T. Felici, "Eigenmode expansion methods for simulation of optical propagation in photonics: pros and cons," in SPIE OPTO, 2003. https://api.semanticscholar.org/CorpusID:110072216

[71] Photon Design, "Photon design - leos newsletter article," IEEE LEOS Newsletter, February 2008. https://www.photond.com/files/docs/leos_newsletter_feb08_article.pdf

[72] K. Kawano and T. Kitoh, Introduction to optical waveguide analysis : solving Maxwell's equations and the Schrodinger equation. J. Wiley, 2001.

[73] K. S. Yee, "Numerical solution of initial boundary value problems involving Maxwell's equations in isotropic media," IEEE Transactions on Antennas and Propagation, vol. 14, pp. 302–307, 1966.

[74] Corning Inc., "Corning® smf-28® ull optical fiber product information," https://www.corning.com/media/worldwide/coc/documents/Fiber/SMF-28%20ULL.pdf, 2020, accessed: 2024-08-14.

[75] Ansys, Inc., "Ansys Lumerical," accessed: 2024-09-12. https://www.ansys.com

[76] J. C. Wirth, "Silicon grating couplers for low loss coupling between optical fiber and silicon nanowires," Master's thesis, Purdue University, West Lafayette, Indiana, Dec 2011, in Partial Fulfillment of the Requirements for the Degree of Master of Science in Electrical and Computer Engineering.

[77] Ansys, Inc., "Symmetric and Anti-Symmetric BCs in FDTD and MODE," accessed: 2024-08-28. https://optics.ansys.com/hc/en-us/articles/360034382694-Symmetric-and-anti-symmetric-BCs-in-FDTD-and-MODE

[78] ——, "EME Solver analysis window overview," Accessed: September 5, 2024. https://optics.ansys.com/hc/en-us/articles/360034917513-EME-Solver-analysis-window-overview

Declaration / Erklärung

Ich versichere, dass ich diese Arbeit selbstständig verfasst und keine anderen als die angegebenen Quellen und Hilfsmittel verwendet habe. Zur Überprüfung der englischen Rechtschreibung dieser Arbeit wurde teilweise ChatGPT verwendet.

Heidelberg, den 26.09.2024,

Inna Shengying Zhang